



HAL
open science

Isoprene photochemistry over the Amazon rainforest

Yingjun Liu, Joel Brito, Matthew R Dorris, Jean C Rivera-Rios, Roger Seco, Kelvin H Bates, Paulo Artaxo, Sergio G Duvoisin, Frank N Keutsch, Saewung Kim, et al.

► **To cite this version:**

Yingjun Liu, Joel Brito, Matthew R Dorris, Jean C Rivera-Rios, Roger Seco, et al.. Isoprene photochemistry over the Amazon rainforest. *Proceedings of the National Academy of Sciences of the United States of America*, 2016, 113 (22), pp.6125 - 6130. 10.1073/pnas.1524136113 . hal-01836099

HAL Id: hal-01836099

<https://uca.hal.science/hal-01836099>

Submitted on 12 Jul 2018

HAL is a multi-disciplinary open access archive for the deposit and dissemination of scientific research documents, whether they are published or not. The documents may come from teaching and research institutions in France or abroad, or from public or private research centers.

L'archive ouverte pluridisciplinaire **HAL**, est destinée au dépôt et à la diffusion de documents scientifiques de niveau recherche, publiés ou non, émanant des établissements d'enseignement et de recherche français ou étrangers, des laboratoires publics ou privés.

Isoprene photochemistry over the Amazon rainforest

Yingjun Liu^a, Joel Brito^b, Matthew R. Dorris^c, Jean C. Rivera-Rios^{c,d}, Roger Seco^e, Kelvin H. Bates^f, Paulo Artaxo^b, Sergio Duvoisin Jr.^g, Frank N. Keutsch^{a,c,d}, Saewung Kim^e, Allen H. Goldstein^h, Alex B. Guenther^{e,i}, Antonio O. Manzi^j, Rodrigo A. F. Souza^k, Stephen R. Springston^l, Thomas B. Watson^l, Karena A. McKinney^{a,1}, and Scot T. Martin^{a,m,1}

^aJohn A. Paulson School of Engineering and Applied Sciences, Harvard University, Cambridge, MA 02138; ^bDepartment of Applied Physics, University of São Paulo, São Paulo 05508, Brazil; ^cDepartment of Chemistry, University of Wisconsin-Madison, Madison, WI 53706; ^dDepartment of Chemistry and Chemical Biology, Harvard University, Cambridge, MA 02138; ^eDepartment of Earth System Science, University of California, Irvine, CA 92697; ^fDivision of Chemistry and Chemical Engineering, California Institute of Technology, Pasadena, CA 91125; ^gDepartment of Chemistry, Universidade do Estado do Amazonas, Manaus, AM 69050, Brazil; ^hDepartment of Environmental Science, Policy, and Management, University of California, Berkeley, CA 94720; ⁱPacific Northwest National Laboratory, Richland, WA 99354; ^jInstituto Nacional de Pesquisas da Amazonia, Manaus, AM 69067, Brazil; ^kDepartment of Meteorology, Universidade do Estado do Amazonas, Manaus, AM 69050, Brazil; ^lDepartment of Environmental and Climate Sciences, Brookhaven National Laboratory, Upton, NY 11973; and ^mDepartment of Earth and Planetary Sciences, Harvard University, Cambridge, MA 02138

Edited by Mark H. Thiemens, University of California, San Diego, La Jolla, CA, and approved April 13, 2016 (received for review December 23, 2015)

Isoprene photooxidation is a major driver of atmospheric chemistry over forested regions. Isoprene reacts with hydroxyl radicals (OH) and molecular oxygen to produce isoprene peroxy radicals (ISOPOO). These radicals can react with hydroperoxyl radicals (HO₂) to dominantly produce hydroxyhydroperoxides (ISOPOOH). They can also react with nitric oxide (NO) to largely produce methyl vinyl ketone (MVK) and methacrolein (MACR). Unimolecular isomerization and bimolecular reactions with organic peroxy radicals are also possible. There is uncertainty about the relative importance of each of these pathways in the atmosphere and possible changes because of anthropogenic pollution. Herein, measurements of ISOPOOH and MVK + MACR concentrations are reported over the central region of the Amazon basin during the wet season. The research site, downwind of an urban region, intercepted both background and polluted air masses during the GoAmazon2014/5 Experiment. Under background conditions, the confidence interval for the ratio of the ISOPOOH concentration to that of MVK + MACR spanned 0.4–0.6. This result implies a ratio of the reaction rate of ISOPOO with HO₂ to that with NO of approximately unity. A value of unity is significantly smaller than simulated at present by global chemical transport models for this important, nominally low-NO, forested region of Earth. Under polluted conditions, when the concentrations of reactive nitrogen compounds were high (>1 ppb), ISOPOOH concentrations dropped below the instrumental detection limit (<60 ppt). This abrupt shift in isoprene photooxidation, sparked by human activities, speaks to ongoing and possible future changes in the photochemistry active over the Amazon rainforest.

isoprene photochemistry | Amazon | organic hydroperoxides

Isoprene (C₅H₈) accounts for approximately half of the global flux of nonmethane biogenic volatile organic compounds to the atmosphere (1). The reactive chemistry of isoprene influences the oxidative capacity of the troposphere and the associated chemical cycles of atmospheric trace gases (2, 3). Isoprene photooxidation products are also important sources of atmospheric organic particulate matter (4–6). Isoprene is mostly oxidized in the atmospheric mixed layer, although entrainment and reaction in the free troposphere can also be important (7, 8).

Isoprene oxidation is mostly initiated by an addition reaction of a photochemically produced hydroxyl radical (OH) across the double bond, followed by the rapid addition of molecular oxygen (O₂) to the primary radical. A population of isoprene peroxy radicals (ISOPOO) is thereby produced. The subsequent chemistry of ISOPOO radicals proceeds along several competing pathways (9). Reaction of ISOPOO with nitric oxide (NO) dominates in polluted regions of the planet. The major products are methyl vinyl ketone (MVK, C₄H₆O) and methacrolein (MACR, C₄H₆O).

The fate of ISOPOO radicals over unpolluted regions of the planet remains unclear. For many isoprene source regions, reaction of ISOPOO with hydroperoxyl radicals (HO₂) has been taken as the dominant pathway (5, 10–13), including over remote tropical

forests like Amazonia where there are few anthropogenic NO sources. The major products of the HO₂ pathway are an isomeric family of hydroxyl hydroperoxides (ISOPOOH; C₅H₁₀O₃). In addition, isomerization and bimolecular reactions with other organic peroxy radicals (RO₂) can also be important (10, 14, 15). Measurements of HO₂, RO₂, and NO, if available, could help to constrain these pathways for unpolluted regions, but each of these measurements is challenging in its own way (16, 17), and available data sets are sparse (2, 18). Unimolecular ISOPOO isomerization, for its part, remains in the early stages of study (10, 15). As a result, the relative contribution of each pathway to the fate of atmospheric ISOPOO radicals remains uncertain for unpolluted regions of Earth (19).

The uncertainty in ISOPOO reaction pathways, in particular the uncertainties of the contributions of NO and HO₂ pathways, hinders accurate prediction of the environmental and climate impacts of isoprene chemistry. The HO₂ reaction pathway is important for the production of particulate matter through second-generation epoxydiol products (5, 6). The NO pathway contributes to the transport of nitrogen beyond the isoprene source region through the formation of stable organic nitrogen compounds (20). The two pathways, to different extents, help to maintain the atmospheric oxidation cycle, including feedbacks on OH and O₃ concentrations (3, 5, 11).

Accurate ambient measurements of the molecular identities and concentrations of isoprene oxidation products are a first-order

Significance

For isolated regions of the planet, organic peroxy radicals produced as intermediates of atmospheric photochemistry have been expected to follow HO₂ rather than NO pathways. Observational evidence, however, has been lacking. An accurate understanding of the relative roles of the two pathways is needed for quantitative predictions of the concentrations of particulate matter, oxidation capacity, and consequent environmental and climate impacts. The results herein, based on measurements, find that the ratio of the reaction rate of isoprene peroxy radicals with HO₂ to that with NO is about unity for background conditions of Amazonia. The implication is that sufficient NO emissions are maintained by natural processes of the forest such that both HO₂ and NO pathways are important, even in this nominally low-NO region.

Author contributions: Y.L., P.A., F.N.K., A.H.G., A.B.G., A.O.M., R.A.F.S., K.A.M., and S.T.M. designed the research; Y.L., J.B., M.R.D., J.C.R., R.S., K.H.B., S.D., S.K., S.R.S., and T.B.W. performed the research; Y.L., K.A.M., and S.T.M. analyzed the data; and Y.L., K.A.M., and S.T.M. wrote the paper.

The authors declare no conflict of interest.

This article is a PNAS Direct Submission.

¹To whom correspondence may be addressed. Email: kamckinney@seas.harvard.edu or scot_martin@harvard.edu.

This article contains supporting information online at www.pnas.org/lookup/suppl/doi:10.1073/pnas.1524136113/-DCSupplemental.

requirement for testing concepts of the reaction pathways of isoprene and the associated predictions of chemical transport models (CTMs). The products MVK and MACR have been studied in many atmospheric environments both by proton transfer reaction mass spectrometry (PTR-MS) and gas chromatography (GC) (21). Large data sets are available (7, 8, 21, 22). By comparison, ambient measurements of ISOPOOH isomers are sparse, and available data sets are limited to temperate regions (23, 24).

An additional issue is that the utility of existing data sets of MVK and MACR concentrations to test and constrain models of isoprene chemistry is challenged by recent laboratory studies that have shown that both PTR-MS and GC techniques can have a contribution from ISOPOOH species in the nominal detection of MVK and MACR (11, 13). For the usual operating conditions of PTR-MS and GC instrumentation, the two main ISOPOOH isomers [specifically, (1-OH, 2-OOH)-ISOPOOH, hereafter (1, 2)-ISOPOOH, and (4-OH, 3-OOH)-ISOPOOH, hereafter (4, 3)-ISOPOOH] decompose on the hot metal surfaces inside both types of instruments (13). The (1, 2)-ISOPOOH and (4, 3)-ISOPOOH decompose to MVK and MACR, respectively. In this case, MVK and MACR concentrations reported in the literature can be expected to be upper limits, rather than best estimates, for regions of Earth where the HO₂ pathway is important for the fate of ISOPOO radicals. On a planetary scale, the contribution of the HO₂ pathway has been modeled as 60% larger than that of the NO pathway (10). The need for corrections to MVK and MACR data sets could be widespread.

In light of these issues, the present study was undertaken to measure the sum of (1, 2)-ISOPOOH and (4, 3)-ISOPOOH concentrations (hereafter, ISOPOOH concentration), in comparison with the sum of MVK and MACR concentrations. The measurements took place in the central region of the Amazon basin during the wet season of 2014. The measurements were made as part of the Observations and Modeling of the Green Ocean Amazon (GoAmazon2014/5) experiment (25). A major concept of the experiment was to locate a research site (T3) several hours downwind of an urban region (specifically, 70 km west of Manaus, Amazonas, Brazil, a city of 2 million people).

Local winds at different times swept either the pollution plume of Manaus or background air of the Amazon basin across the research site. As a result, the species observed at T3 were at times produced upwind under background conditions whereas, at other times, they were significantly affected by pollution. Based on back-trajectories, the most probable transport time from the city to the measurement site was between 4 h and 5 h. By comparison, (4, 3)-ISOPOOH, isoprene, (1, 2)-ISOPOOH, MACR, and MVK have characteristic lifetimes to OH loss of ~2 h, 3 h, 4 h, 10 h, and 14 h, respectively, for a reference OH concentration of 10⁶ cm⁻³ typical of many environments. Deposition and entrainment can also be important loss mechanisms (26, 27). Background air, meaning the Amazon basin in the nominal absence of the pollution plume of Manaus, had significant variability associated with it, especially with respect to effective photochemical age. Background variability arose from variations of in-basin emissions and transformations integrated across several days of meteorology as well as, at times, from significant out-of-basin influences and variability tied to transport from the Atlantic Ocean and Africa (28, 29). Even so, the effect of the plume, when present, dominated over this background variability for the measured quantities of the present study. Measurements of the ratio of ISOPOOH to MVK + MACR concentrations, reported herein, are used to assess how different amounts of pollution, including background conditions in the absence of anthropogenic influence (i.e., low NO), regulate the relative importance of isoprene photooxidation pathways in the tropical forest of central Amazonia.

Observations

Data sets were collected at the T3 site of GoAmazon2014/5 in the wet season during an 8-week intensive operating period (*SI Appendix*). Concentrations of ISOPOOH and MVK + MACR were measured using a proton transfer reaction time-of-flight mass spectrometer (PTR-TOF-MS). ISOPOOH and MVK + MACR, both detected as the C₄H₇O⁺ ion by the PTR-TOF-MS, were discriminated by use of an upstream cold trap. ISOPOOH, having a lower volatility than does MVK or MACR, was selectively removed by the cold trap (11, 30).

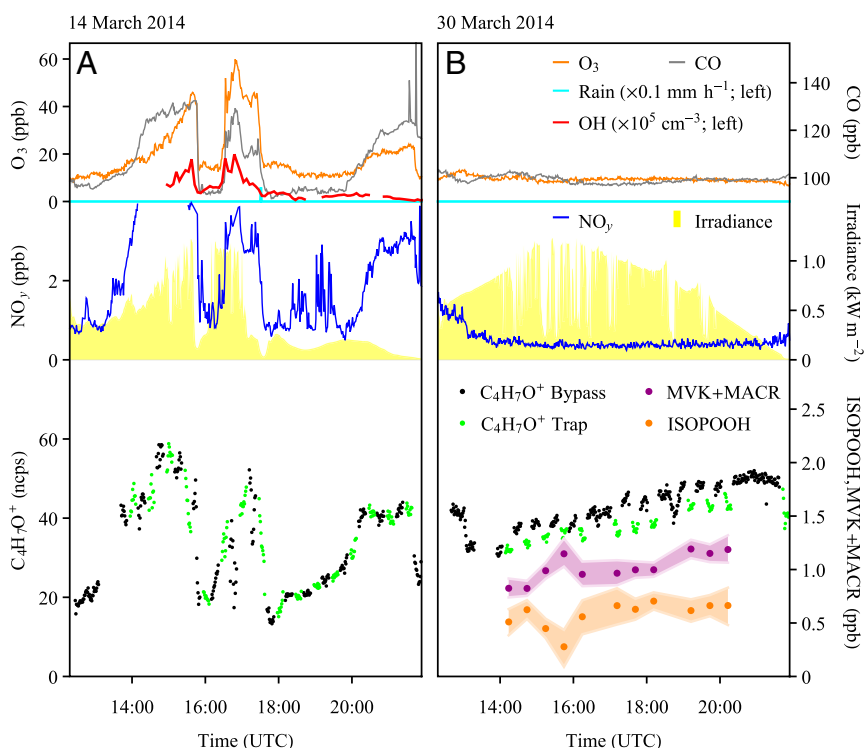


Fig. 1. Representative afternoon time series of (*Top*) CO concentrations, O₃ concentrations, OH concentrations, and rain amount; (*Middle*) NO_y concentrations and shortwave broadband total down-welling irradiance; and (*Bottom*) signal intensities of C₄H₇O⁺ ions and concentrations of MVK+MACR and ISOPOOH. Lifetimes of CO, O₃, and OH are many days, many hours, and less than 1 s, respectively, over the tropical forest in Amazonia. (A) Polluted conditions (14 March 2014). The weather was partly cloudy with scattered showers. (B) Background conditions (30 March 2014). The weather was sunny, and there was no rainfall. Local noon is at 1600 UTC. The green and black points for the C₄H₇O⁺ ions represent intensities with and without the cold trap in place, respectively. Intensities are given in normalized counts per second (ncps) (*SI Appendix*). For concentrations of MVK + MACR and ISOPOOH, the light shadings represent 75% confidence intervals. Measurements of OH concentrations are not available for 30 March 2014.

Fig. 1 shows the time series of trap and bypass signal intensities of the $C_4H_7O^+$ ion for two contrasting afternoons. The time series of the concentrations of reactive nitrogen compounds (NO_y), ozone (O_3), and carbon monoxide (CO) show that Fig. 1 *A* and *B* correspond, respectively, to time periods when the pollution plume or background air passed over T3. The NO_y concentration is defined as the sum concentration of NO, NO_2 , and compounds produced from them. NO_y favors NO and NO_2 near source regions and remains a semiconserved quantity downwind as NO and NO_2 are incorporated into product molecules. The instantaneous concentrations of NO at T3 are often below detection limit [70 parts per trillion (ppt)] because of the rapid titration of this species by peroxy radicals and ozone, even as it remains an important reactant. For these reasons, NO_y concentration is used in this study as a surrogate variable for the integrated effects of NO on the chemistry that took place during transport to T3. As a reference point, background air in the boundary layer of the central Amazon basin in the wet season is characterized by 0.5 ± 0.3 parts per billion (ppb) of NO_y (31).

On the afternoon affected by pollution, the NO_y concentrations measured at T3 were regularly above 1 ppb (Fig. 1*A*, *Middle*). The concentrations of O_3 and CO were also elevated (Fig. 1*A*, *Top*). Back-trajectories from T3 show that the air came from Manaus (*SI Appendix*, Fig. S1*A*). Under the influence of this pollution, the trap and bypass intensities for the $C_4H_7O^+$ ion followed each other closely (Fig. 1*A*, *Bottom*), without any statistically significant differences. The conclusions for this polluted afternoon are that the NO pathway dominated over the HO_2 pathway for the fate of ISOPOO radicals and that the $C_4H_7O^+$ intensity predominantly arose from MVK and MACR, without any contribution by ISOPOOH.

Fluctuations are apparent in the data sets of Fig. 1*A* at several time points throughout the day. The fluctuations at 1600 UTC arose from a 45-min shift in the local winds from polluted easterlies to background southerlies associated with a local convective cell (*SI Appendix*, Fig. S2). Atmospheric concentrations of the measured species decreased because of a combination of wet deposition and convective mixing with clean air. The precipitous drops in the data sets at 1745 UTC were associated with rainfall. At other times, small fluctuations reflected variations in the amounts of Manaus pollution that reached the measurement site during the course of the observations. The $C_4H_7O^+$ intensity fluctuated in correlation with the NO_y concentration (Fig. 1*A*, *Middle* compared with *Bottom*). MVK and MACR were produced more rapidly in air masses having higher NO_y concentrations because the atmospheric oxidation cycle was accelerated (32). As an example of this acceleration, the instantaneous OH concentration increased markedly when pollution and sunlight were simultaneously present (Fig. 1*A*, *Top*).

During the afternoon of background conditions, the NO_y concentration at T3 varied little from 0.4 ppb throughout the day (Fig. 1*B*, *Middle*). Ozone and carbon monoxide had concentrations typical of background air masses in the wet season (Fig. 1*B*, *Top*) (29). Back-trajectories launched from T3 showed that the air did not intersect Manaus. The air instead came from remote regions of the Amazon basin (*SI Appendix*, Fig. S1*B*). Under these conditions, the HO_2 pathway played an important role in the fate of ISOPOO radicals, and, on this afternoon, the $C_4H_7O^+$ intensity with the cold trap in place was lower than in its absence (Fig. 1*B*, *Bottom*).

A difference signal $\Delta C_4H_7O^+$ measured with and without the trap can be defined (*SI Appendix*). A nonzero $\Delta C_4H_7O^+$ is attributed to the presence of ISOPOOH (11). The possibility of significant contributions by other compounds to $\Delta C_4H_7O^+$, such as pinonaldehyde and isoprene epoxydiols (IEPOX) (30), was considered but ruled out (*SI Appendix*). The difference signal $\Delta C_4H_7O^+$ was converted to ISOPOOH concentration based on calibrations using synthesized standards of ISOPOOH isomers. The MVK+MACR concentration was subsequently determined. For the afternoon of background conditions, the ISOPOOH concentration was ~ 0.6 ppb throughout

the day (Fig. 1*B*, *Bottom*). The MVK + MACR concentration increased from 0.9 ppb to 1.2 ppb. For comparison, daytime ISOPOOH concentrations in the western United States of up to 1 ppb were reported using CF_3O^- as the ionization agent in a chemical ionization mass spectrometer, although authentic standards were not available for instrument calibration (23). A similar instrument, but with calibration, subsequently measured 0.4 ppb as the daytime ISOPOOH + IEPOX concentration in the southeastern United States (24).

Twenty-three days of daytime trap data were obtained during the measurement period, and a statistical analysis was carried out (Fig. 2). The $\Delta C_4H_7O^+$ values were grouped by NO_y concentration such that each of the six data subsets had an equal number of data points. Quartile and median values of $\Delta C_4H_7O^+$ intensity and NO_y concentration were calculated for each subset. Results are plotted in Fig. 2*A*. For subsets of $NO_y > 1$ ppb, indicating the influence of the Manaus pollution plume, the medians were approximately zero (Fig. 2*A*), meaning that no ISOPOOH was detected for these conditions. By comparison, for subsets having $NO_y < 1$ ppb, indicating the sampling of background air, the medians increased for decreasing NO_y concentration. The implication is that ISOPOOH concentrations increased with lower NO_y concentrations.

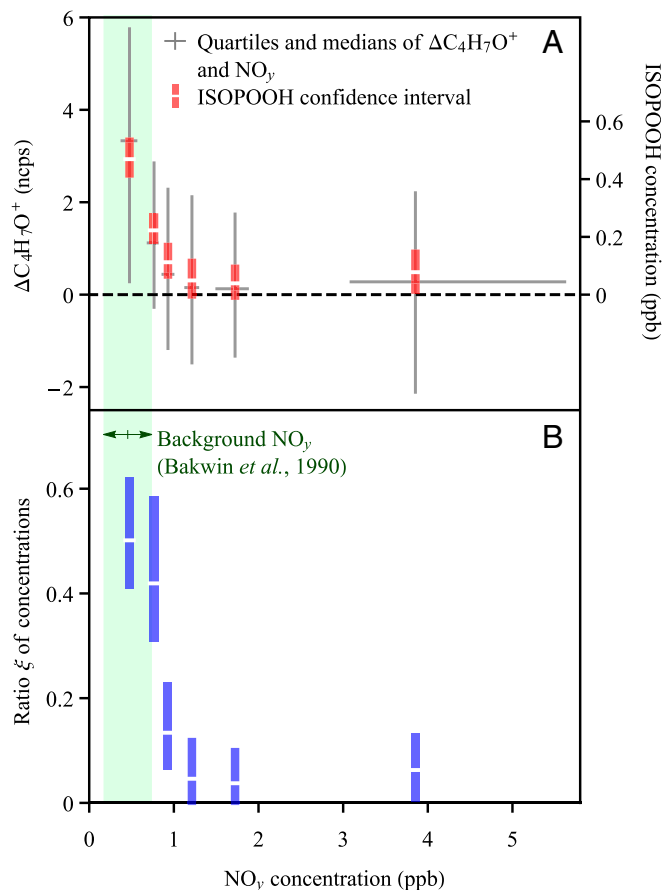


Fig. 2. Dependence of observations on NO_y concentration. (A) Quartiles and median of $\Delta C_4H_7O^+$ measurements. The central value of the ISOPOOH concentration, corresponding to the median of the $\Delta C_4H_7O^+$ measurements, is also shown. The bar represents the 75% confidence interval around the central value of the obtained ISOPOOH concentration. (B) Ratio ξ of ISOPOOH concentration to that of MVK + MACR. The central value of the ratio is based on the median of the $\Delta C_4H_7O^+$ measurements. The bar represents the 75% confidence interval around the central value of the obtained ratio. Light green shading represents NO_y concentrations of background air masses in the central Amazon basin in the wet season (31).

The central values of the ISOPOOH concentrations derived from the median values of the $\Delta\text{C}_4\text{H}_7\text{O}^+$ measurements are represented on the right axis of Fig. 2A. The bar represents the 75% confidence interval around the central value of the obtained ISOPOOH concentration. Medians of $\Delta\text{C}_4\text{H}_7\text{O}^+$ (left axis) and central values of ISOPOOH concentrations (right axis) are slightly offset from one another because of nonlinearity in the ISOPOOH calibration, including a dependence on humidity (*SI Appendix*). For the bin of lowest NO_y concentration, which corresponds to 0.5 ppb as a median value, the central value of the ISOPOOH concentration was 0.5 ppb. This NO_y bin is coincident with the envelope of 0.5 ± 0.3 ppb characteristic of background conditions in the wet season of Amazonia (31).

The concentration of ISOPOOH compared with that of MVK + MACR, represented as a ratio quantity ξ , was calculated, and its relationship to NO_y was analyzed. Fig. 2B plots the central value of ξ and its 75% confidence interval (bar length) for each NO_y bin. The ratio ξ decreases for increasing NO_y concentration, approaching zero for $\text{NO}_y > 1$ ppb. For the lowest NO_y concentration, characteristic of background conditions, the central value of ξ was 0.5 (0.4–0.6 with uncertainty).

From a technical perspective, ξ can indicate the possible quantitative error in the historical assumption that the $\text{C}_4\text{H}_7\text{O}^+$ signal arose exclusively from MVK and MACR. Fig. 2B shows that ξ changed with NO_y concentration for $\text{NO}_y < 1$ ppb but was close to zero for $\text{NO}_y > 1$ ppb. A criterion of $\text{NO}_y > 1$ ppb is, therefore, suggested as a simple heuristic check before attributing the $\text{C}_4\text{H}_7\text{O}^+$ signal in future studies exclusively to MVK and MACR concentrations. This heuristic applies assuming that the dependence observed in the wet season of the central Amazon basin also applies to other environments. More generally, a confidence interval of 0.4–0.6 for ξ under background conditions in central Amazonia suggests that the nominal MVK and MACR concentrations reported in the literature for remote locations are in need of correction for ISOPOOH contributions when PTR-MS, GC, or other methods having hot metal surfaces were used for the measurements.

Modeling

The observed concentration ratio ξ can be used in an analytical model to estimate the ratio χ of the production rate of ISOPOOH to that of MVK + MACR. This ratio corresponds to $(S_1 + S_2)/(S_3 + S_4)$ for production rates S_i (molec $\text{cm}^{-3} \text{s}^{-1}$) of species i . Species 1–4 correspond to (1, 2)-ISOPOOH, (4, 3)-ISOPOOH, MVK, and MACR, respectively. Quantities ξ and χ differ from one another because of the different atmospheric lifetimes of species i . For initial concentrations of zero and for production rates S_i and loss coefficients k_i (s^{-1}) that are constant, the following result can be obtained to relate χ to ξ for a reaction time t (*SI Appendix*):

$$\chi = \frac{(0.6/k_3)(1 - e^{-k_3t}) + (0.4/k_4)(1 - e^{-k_4t})}{(0.6/k_1)(1 - e^{-k_1t}) + (0.4/k_2)(1 - e^{-k_2t})} \xi. \quad [1]$$

Composite, pseudo-first-order loss coefficients k_i are given by $k_i = k_{i,\text{OH}}[\text{OH}] + k_{i,\text{en}} + k_{i,d}$ for bimolecular reactions with OH, atmospheric entrainment (*en*), and surface deposition (*d*). On-site measurements of OH concentrations by chemical ionization mass spectrometry (33), recent advances in the understanding of the deposition processes of ISOPOOH (26), and an approximate description of the boundary layer dynamics over the Amazonia (34) allow reasonable estimates of the loss coefficients k_i (*SI Appendix, Table S1*).

The model derivation relies on the accuracy of two approximations. (i) Species concentrations are taken as zero at sunrise, which then represents time zero. This approximation is well supported by measured concentrations, which at sunrise were $< 5\%$ of the maximum measured daily concentrations (*SI Appendix, Fig. S3*). (ii)

Production rates S_i and loss coefficients k_i are approximated as constant throughout the day, thereby corresponding to average or effective daily values. The sensitivity of the results to this approximation is examined in *SI Appendix*.

Eq. 1 shows that the production ratio χ is proportional to the concentration ratio ξ for any fixed reaction time. For an average daytime OH concentration of $5 \times 10^5 \text{ cm}^{-3}$ for background conditions (33) and an effective reaction time of 5 h representing day-break to midafternoon, the proportionality coefficient is 1.5 (*SI Appendix, Fig. S4*). The confidence interval of 0.4–0.6 for ξ under background conditions (Fig. 2B) implies a range of 0.6–0.9 for χ . The appropriateness of the effective photochemical reaction time (i.e., $5 \times 10^5 \text{ OH cm}^{-3}$ for 5 h) is verified by the agreement of the predicted and measured ratios given by the total concentration of reaction products (i.e., sum of MVK, MACR, and ISOPOOH) divided by the isoprene concentration (*SI Appendix*).

The product-focused methodology to determine χ can be complemented by a source-based analysis. Reactions of ISOPOOH as the sources of ISOPOOH and MVK + MACR. In a source-based analysis, the production ratio χ is expressed as follows:

$$\chi = \frac{Y_{\text{ISOPOOH, HO}_2} f_{\text{HO}_2}}{\sum_{j \in \{\text{HO}_2, \text{NO}, \text{RO}_2, \text{ISOM}\}} Y_{\text{MVK+MACR, } j} f_j} \quad [2]$$

The fractional yield of ISOPOOH in the reaction of ISOPOOH with HO_2 is represented by the term $Y_{\text{ISOPOOH, HO}_2}$, which has an estimated value of 0.90 (35). By comparison, ISOPOOH is believed to be produced neither from the reactions of ISOPOOH with NO and RO_2 nor by isomerization. The fraction yield of MVK + MACR in pathway j of the ISOPOOH reaction is represented by the term $Y_{\text{MVK+MACR, } j}$. The best-estimate values for NO, HO_2 , RO_2 and isomerization (ISOM) pathways are 0.06, 0.71, 0.75, and 0.10, respectively (*SI Appendix, Table S2* and references therein).

Term f_j of Eq. 2 is the fractional contribution of pathway j to ISOPOOH loss. The fractions of the NO, HO_2 , RO_2 , and isomerization pathways sum to unity. These fractions were obtained for NO concentrations ranging from background to polluted conditions using a box model based on the Master Chemical Mechanism (version 3.3.1) and supplemented by recent experimental results (9, 11, 35). For straightforwardness, the OH concentration was held constant, although, in reality, it increased under polluted conditions (Fig. 1A). Fig. 3A shows the simulated dependence of f_{HO_2} , f_{NO} , f_{RO_2} , and f_{ISOM} on NO concentration. Under polluted conditions of greater than several hundred ppt of NO, ISOPOOH loss is dominated by reaction with NO (e.g., 90% for 400 ppt NO). Under less polluted conditions, the other three reaction pathways become important.

Fig. 3B shows the simulated dependence of production ratio χ on NO concentration and allows an inference of an effective NO concentration associated with the confidence interval 0.6–0.9 for χ . As a point of reference, background NO mixing ratios of 15–60 ppt (36), 10–30 ppt (37), 20–80 ppt (31), and 35 ppt (mean value of GoAmazon2014/5 aircraft measurement; *SI Appendix, Fig. S5*) have been measured for the central region of the Amazon basin for studies from 1985 through 2014. These ranges are represented by the brown arrows in Fig. 3B. According to Fig. 3B, the effective NO concentration associated with the confidence interval of χ ranged from 16 to 30 ppt (Fig. 3, yellow shading). This effective value represents the net chemistry across the history of the air parcel. The good agreement between the effective NO concentration inferred in this way and the range of measured ambient concentrations for background conditions lends confidence to the accuracy of the overall model framework of the present study. Across the range of effective NO concentrations, the following fractional contributions to ISOPOOH reaction are obtained: $0.31 < f_{\text{HO}_2} < 0.39$, $0.27 < f_{\text{NO}} < 0.40$, $0.03 < f_{\text{RO}_2} < 0.05$, and $0.25 < f_{\text{ISOM}} < 0.30$ (Fig. 3A, yellow

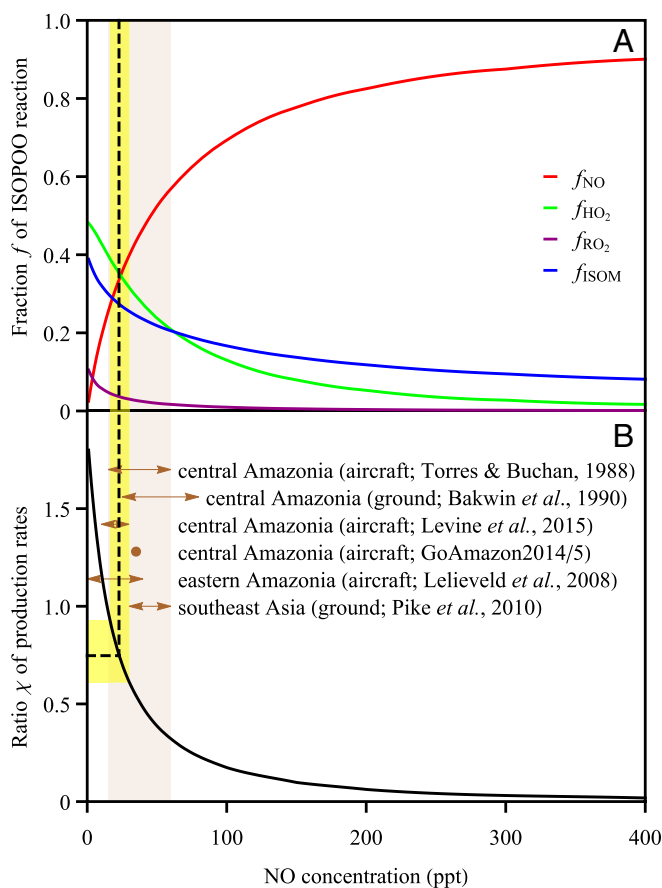


Fig. 3. Modeled dependence on NO concentration of (A) fractional contributions f_{HO_2} , f_{NO} , f_{RO_2} , and f_{ISOM} to ISOPOO reactive loss and (B) the ratio χ of the production rate of ISOPOOH to that of MVK + MACR. The brown arrows represent the reported ranges of NO concentration for central Amazonia, eastern Amazonia, and southeast Asia under background conditions (2, 31, 36, 37, 48). The gray region represents NO concentrations reported by Torres and Buchan (36) for measurements in 1985. The dashed line projects the central value of χ for background conditions onto the effective NO concentration, illustrating the possible relative contributions of different reaction pathways of ISOPOO. The yellow region shows the same as the dashed line but for confidence interval in χ .

shading). Notably, compared with the wide range of NO concentrations reported (Fig. 3A, gray shading), the effective NO concentrations based on our observation provide a tighter constraint to ISOPOO reaction under background conditions. Specifically, the confidence interval of the f_{HO_2} -to- f_{NO} ratio spans 0.8–1.4. This result is robust with respect to the inclusion or not of the isomerization pathway (SI Appendix, Table S3). An important point to emphasize is that the modeling analysis leading to this ratio for background conditions is ultimately constrained by the measured concentrations of ISOPOOH, MVK + MACR, and NO_x .

Implications

The ranges in f_{NO} , f_{HO_2} , f_{RO_2} , and f_{ISOM} for the yellow region of Fig. 3A imply that the HO_2 pathway accounted for 31–39% of the reactive loss of ISOPOO under the low-NO conditions of the wet season in the central Amazon basin. Conversely, reactions with NO under low-NO conditions accounted for 27–40% of ISOPOO loss. For comparison with these values, a state-of-the-art CTM predicted that the HO_2 pathway contributed 59% of the reactive loss of ISOPOO radicals for the grid box of $4^\circ \times 5^\circ$ encompassing the measurement site and that the contribution of the NO pathway to reactive loss was 14% for a typical wet season (SI Appendix,

Table S4). An overestimate in models of the importance of the HO_2 pathway for ISOPOO reactive loss has important implications for predicted concentrations of organic particulate matter (5) and consequent connections among flora, oxidative capacity, aerosol particles, cloud condensation nuclei, clouds, and rainfall over this vast tropical forest (38). An underestimate of the NO pathway in central Amazonia can have profound impacts on the predicted concentrations of isoprene nitrates transported to adjacent regions, influencing NO_x concentrations and photochemistry in those regions (39). In addition, given the importance of this geographical region in the global isoprene budget (1), previous estimates of the fraction of ISOPOO reacting via the HO_2 pathway on a global basis by CTMs might also be too high (10). Future studies are needed to better constrain the fraction of ISOPOO reactive loss via the HO_2 pathway in other locations having high isoprene concentrations and low anthropogenic NO_x emissions.

One possible reason, among others, for the gap between observations and the CTM model predictions is an underprediction of NO concentrations and hence an underestimate of the importance of the NO reaction pathway in the model. The modeled daytime average concentration of NO was 8 ppt for the grid box in which the measurement site was located. This value is much lower than the range of NO concentrations measured in central Amazonia (Fig. 3). Furthermore, the modeled daytime concentration of NO_y was 0.1 ppb, which is 80% lower than the observed background NO_y concentrations in central Amazonia (31). Underpredicted NO and NO_y concentrations in the model might, in turn, be related to underestimated NO emissions from tropical forests. Flux measurements have shown that soils have high emissions of NO_x in the forested regions of both central Amazonia (40–43) and southeast Asia (44). The above-soil NO_x emission modeled in the CTM for the wet season of central Amazonia was 10 times lower than the observations reported in the literature (SI Appendix). Ganzeveld et al. (45) additionally suggest that CTMs might underestimate the fraction of soil-emitted NO_x that survives transport through tropical forest layers and is ultimately emitted to the overlying atmosphere. Herein, additional model runs were performed as a sensitivity study to establish that increasing NO_x emissions above canopy by a factor of 30 can bring the modeled ratio ξ closer to its observed range (SI Appendix). Any change made to model emissions on this basis must, however, also assess possible perturbations of other modeled quantities, such as ozone and hydroxyl radical concentrations, compared with measured values (2, 46).

In outlook, current trends in human activities, including ongoing land use changes for agricultural activities as well as growing urbanization, are associated with the continual reduction of forest coverage in the Amazon basin (47). These trends, in turn, lead to increased demand for electricity and transport, which, with current technologies, increases NO_x emissions (44). With respect to the atmospheric chemistry of the region, the concentration ratio ξ and its complement of the production ratio χ serve as surrogates of the qualitative characteristics of isoprene chemistry, with associated effects that are of concern to humans, such as production of ozone and organic particulate matter and changes in visibility and rainfall, among others (3, 38). Under background conditions, expressed as 75% confidence intervals, the ratio of the fractional contribution by HO_2 to the reactive loss of ISOPOO to that by NO ranges from 0.8 to 1.4, the ratio of the production rate χ of ISOPOOH to that of MVK + MACR ranges from 0.6 to 0.9, and the ratio ξ of the concentration of ISOPOOH to that of MVK + MACR ranges from 0.4 to 0.6. In this regard, the data (Fig. 2, ξ) and the model (Fig. 3, χ) show that the oxidant cycle is highly sensitive to changes from background to polluted conditions. The implication is that small increases in NO concentration above the background level can lead to a large change in the aforementioned endpoints of air quality and climate. In particular, the abrupt drop in ISOPOOH concentration associated with pollution speaks to the extent of

human-induced changes in photochemical cycles over the rain forest, both at present during times of widespread biomass burning in the dry season and, possibly, in the future during all seasons as a consequence of economic development and increasing pollution throughout the Amazon basin.

Materials and Methods

Measurements were made at the T3 site of the GoAmazon2014/5 Experiment (25). A PTR-TOF-MS (Ionicon Analytik) equipped with a cold trap was used to measure ISOPOOH and MVK + MACR concentrations. The approach was to collect data for a period with the trap in line to quantify MVK+MACR followed by a period in bypass to quantify MVK+MACR+ISOPOOH. Detailed additional information about the measurements and associated modeling is provided in *SI Appendix*.

- Guenther A, et al. (2012) The Model of Emissions of Gases and Aerosols from Nature version 2.1 (MEGAN2.1): An extended and updated framework for modeling biogenic emissions. *Geosci Model Dev* 5(6):1471–1492.
- Lelieveld J, et al. (2008) Atmospheric oxidation capacity sustained by a tropical forest. *Nature* 452(7188):737–740.
- Chameides WL, Lindsay RW, Richardson J, Kiang CS (1988) The role of biogenic hydrocarbons in urban photochemical smog: Atlanta as a case study. *Science* 241(4872):1473–1475.
- Claeys M, et al. (2004) Formation of secondary organic aerosols through photooxidation of isoprene. *Science* 303(5661):1173–1176.
- Paulot F, et al. (2009) Unexpected epoxide formation in the gas-phase photooxidation of isoprene. *Science* 325(5941):730–733.
- Surratt JD, et al. (2010) Reactive intermediates revealed in secondary organic aerosol formation from isoprene. *Proc Natl Acad Sci USA* 107(15):6640–6645.
- Karl T, et al. (2007) The tropical forest and fire emissions experiment: Emission, chemistry, and transport of biogenic volatile organic compounds in the lower atmosphere over Amazonia. *J Geophys Res* 112(D18):D18302.
- Kuhn U, et al. (2007) Isoprene and monoterpene fluxes from Central Amazonian rainforest inferred from tower-based and airborne measurements, and implications on the atmospheric chemistry and the local carbon budget. *Atmos Chem Phys* 7(11):2855–2879.
- Jenkin ME, Young JC, Rickard AR (2015) The MCM v3.3.1 degradation scheme for isoprene. *Atmos Chem Phys* 15(20):11433–11459.
- Crouse JD, Paulot F, Kjaergaard HG, Wennberg PO (2011) Peroxy radical isomerization in the oxidation of isoprene. *Phys Chem Chem Phys* 13(30):13607–13613.
- Liu YJ, Herdinger-Blatt I, McKinney KA, Martin ST (2013) Production of methyl vinyl ketone and methacrolein via the hydroperoxyl pathway of isoprene oxidation. *Atmos Chem Phys* 13(11):5715–5730.
- Chen Q, et al. (2015) Submicron particle mass concentrations and sources in the Amazonian wet season (AMAZE-08). *Atmos Chem Phys* 15(7):3687–3701.
- Rivera-Rios JC, et al. (2014) Conversion of hydroperoxides to carbonyls in field and laboratory instrumentation: Observational bias in diagnosing pristine versus anthropogenically controlled atmospheric chemistry. *Geophys Res Lett* 41(23):8645–8651.
- Jenkin ME, Boyd AA, Lesclaux R (1998) Peroxy radical kinetics resulting from the OH-initiated oxidation of 1,3-butadiene, 2,3-dimethyl-1,3-butadiene and isoprene. *J Atmos Chem* 29(3):267–298.
- Peeters J, Müller J-F, Stavroukaki T, Nguyen VS (2014) Hydroxyl radical recycling in isoprene oxidation driven by hydrogen bonding and hydrogen tunneling: The up-graded LIM1 mechanism. *J Phys Chem A* 118(38):8625–8643.
- Fuchs H, et al. (2011) Detection of HO₂ by laser-induced fluorescence: Calibration and interferences from RO₂ radicals. *Atmos Meas Tech* 4(6):1209–1225.
- Hoell JM, et al. (1987) Airborne intercomparison of nitric oxide measurement techniques. *J Geophys Res* 92(D2):1995–2008.
- Hewitt CN, et al. (2010) Overview: oxidant and particle photochemical processes above a south-east Asian tropical rainforest (the OP3 project): Introduction, rationale, location characteristics and tools. *Atmos Chem Phys* 10(1):169–199.
- Wennberg PO (2013) Let's abandon the "high NO_x" and "low NO_x" terminology. *IGAC News* 50:3–4.
- Perring AE, Pusede SE, Cohen RC (2013) An observational perspective on the atmospheric impacts of alkyl and multifunctional nitrates on ozone and secondary organic aerosol. *Chem Rev* 113(8):5848–5870.
- de Gouw J, Warneke C (2007) Measurements of volatile organic compounds in the Earth's atmosphere using proton-transfer-reaction mass spectrometry. *Mass Spectrom Rev* 26(2):223–257.
- Karl T, et al. (2009) Rapid formation of isoprene photo-oxidation products observed in Amazonia. *Atmos Chem Phys* 9(20):7753–7767.
- Worton DR, et al. (2013) Observational insights into aerosol formation from isoprene. *Environ Sci Technol* 47(20):11403–11413.
- Xiong F, et al. (2015) Observation of isoprene hydroxynitrates in the southeastern United States and implications for the fate of NO_x. *Atmos Chem Phys* 15(19):11257–11272.
- Martin ST, et al. (2016) Introduction: Observations and Modeling of the Green Ocean Amazon (GoAmazon2014/5). *Atmos Chem Phys* 16(8):4785–4797.
- Nguyen TB, et al. (2015) Rapid deposition of oxidized biogenic compounds to a temperate forest. *Proc Natl Acad Sci USA* 112(5):E392–E401.
- Karl T, et al. (2013) Airborne flux measurements of BVOCs above Californian oak forests: Experimental investigation of surface and entrainment fluxes, OH densities, and Damköhler numbers. *J Atmos Sci* 70(10):3277–3287.
- Chen Q, et al. (2009) Mass spectral characterization of submicron biogenic organic particles in the Amazon Basin. *Geophys Res Lett* 36(20):L20806.
- Martin ST, et al. (2010) Sources and properties of Amazonian aerosol particles. *Rev Geophys* 48(2):RG2002.
- Nguyen TB, et al. (2014) Overview of the Focused Isoprene eXperiment at the California Institute of Technology (FIXCIT): Mechanistic chamber studies on the oxidation of biogenic compounds. *Atmos Chem Phys* 14(24):13531–13549.
- Bakwin PS, Wofsy SC, Fan S-M (1990) Measurements of reactive nitrogen oxides (NO_x) within and above a tropical forest canopy in the wet season. *J Geophys Res* 95(D10):16765–16772.
- Valin LC, Russell AR, Cohen RC (2013) Variations of OH radical in an urban plume inferred from NO₂ column measurements. *Geophys Res Lett* 40(9):1856–1860.
- Kim S, et al. (2013) Evaluation of HO₂ sources and cycling using measurement-constrained model calculations in a 2-methyl-3-butene-2-ol (MBO) and monoterpene (MT) dominated ecosystem. *Atmos Chem Phys* 13(4):2031–2044.
- Vilà-Guerau de Arellano J, van den Dries K, Pino D (2009) On inferring isoprene emission surface flux from atmospheric boundary layer concentration measurements. *Atmos Chem Phys* 9(11):3629–3640.
- St Clair JM, et al. (2016) Kinetics and products of the reaction of the first-generation isoprene hydroxy hydroperoxide (ISOPOOH) with OH. *J Phys Chem A* 120(9):1441–1451.
- Torres AL, Buchan H (1988) Tropospheric nitric oxide measurements over the Amazon Basin. *J Geophys Res* 93(D2):1396–1406.
- Levine JG, et al. (2015) Isoprene chemistry in pristine and polluted Amazon environments: Eulerian and Lagrangian model frameworks and the strong bearing they have on our understanding of surface ozone and predictions of rainforest exposure to this priority pollutant. *Atmos Chem Phys Discuss* 15(17):24251–24310.
- Pöschl U, et al. (2010) Rainforest aerosols as biogenic nuclei of clouds and precipitation in the Amazon. *Science* 329(5998):1513–1516.
- Ito A, Sillman S, Penner JE (2007) Effects of additional nonmethane volatile organic compounds, organic nitrates, and direct emissions of oxygenated organic species on global tropospheric chemistry. *J Geophys Res* 112(D6):D06309.
- Bakwin PS, et al. (1990) Emission of nitric oxide (NO) from tropical forest soils and exchange of NO between the forest canopy and atmospheric boundary layers. *J Geophys Res* 95(D10):16755–16764.
- Verchot LV, et al. (1999) Land use change and biogeochemical controls of nitrogen oxide emissions from soils in eastern Amazonia. *Global Biogeochem Cycles* 13(1):31–46.
- García-Montiel DC, et al. (2001) Controls on soil nitrogen oxide emissions from forest and pastures in the Brazilian Amazon. *Global Biogeochem Cycles* 15(4):1021–1030.
- Kaplan WA, Wofsy SC, Keller M, Da Costa JM (1988) Emission of NO and deposition of O₃ in a tropical forest system. *J Geophys Res* 93(D2):1389–1395.
- Hewitt CN, et al. (2009) Nitrogen management is essential to prevent tropical oil palm plantations from causing ground-level ozone pollution. *Proc Natl Acad Sci USA* 106(44):18447–18451.
- Ganzeveld LN, et al. (2002) Global soil-biogenic NO_x emissions and the role of canopy processes. *J Geophys Res* 107(D16):4298.
- Jacob DJ, Wofsy SC (1988) Photochemistry of biogenic emissions over the Amazon forest. *J Geophys Res* 93(D2):1477–1486.
- Davidson EA, et al. (2012) The Amazon basin in transition. *Nature* 481(7381):321–328.
- Pike RC, et al. (2010) NO_x and O₃ above a tropical rainforest: An analysis with a global and box model. *Atmos Chem Phys* 10(21):10607–10620.

SI Appendix

Isoprene Photochemistry over the Amazon Rain Forest

by

Yingjun Liu^a, Joel Brito^b, Matthew R. Dorris^c, Jean C. Rivera-Rios^{c,d}, Roger Seco^e, Kelvin H. Bates^f, Paulo Artaxo^b, Sergio Duvoisin Jr.^g, Frank N. Keutsch^{a,c,d}, Saewung Kim^e, Allen H. Goldstein^h, Alex B. Guenther^{e,i}, Antonio O. Manzi^j, Rodrigo A. F. Souza^k, Stephen R. Springston^l, Thomas B. Watson^l, Karena A. McKinney^{a,1}, Scot T. Martin^{a,m,1}

^a John A. Paulson School of Engineering and Applied Sciences, Harvard University, Cambridge, MA 02138;

^b Department of Applied Physics, University of São Paulo, São Paulo 05508, Brazil;

^c Department of Chemistry, University of Wisconsin-Madison, Madison, WI 53706;

^d Department of Chemistry and Chemical Biology, Harvard University, Cambridge, MA 02138;

^e Department of Earth System Science, University of California, Irvine, CA 92697;

^f Division of Chemistry and Chemical Engineering, California Institute of Technology, Pasadena, CA 91125;

^g Department of Chemistry, Universidade do Estado do Amazonas, Manaus, AM 69050, Brazil;

^h Department of Environmental Science, Policy, and Management, University of California, Berkeley, CA 94720;

ⁱ Pacific Northwest National Laboratory, Richland, WA 99354;

^j Instituto Nacional de Pesquisas da Amazonia, Manaus, AM 69067, Brazil;

^k Department of Meteorology, Universidade do Estado do Amazonas, Manaus, AM 69050, Brazil;

^l Department of Environmental and Climate Sciences, Brookhaven National Laboratory, Upton, NY 11973;

^m Department of Earth and Planetary Sciences, Harvard University, Cambridge, MA 02138.

Proceedings of the National Academy of Sciences

¹To Whom Correspondence Should be Addressed

E-mail: scot_martin@harvard.edu, kamckinney@seas.harvard.edu

1. Experiments and data analysis

Measurements were made at the T3 site of the GoAmazon2014/5 Experiment (1). The site T3 was located in a pasture area of 2.5 km × 2 km (-3.2133°, -60.5987°). Pasture regions have low emissions of isoprene (2), and the isoprene observed at T3 originated predominantly from the upwind forest. The fetch of the T3 site oscillated between the extremes of a background atmosphere and influences of Manaus pollution depending on the deflection of trade winds slightly to the north or south with daily weather. At T3, a research container, part of the Mobile Aerosol Observing System (MAOS) of the USA Department of Energy, housed instrumentation (www.arm.gov). The main trace-gas inlet (12.7-mm PFA; 13 sLpm) was 10 m above the ground.

A proton-transfer-reaction time-of-flight mass spectrometer (PTR-TOF-MS, Ionicon Analytik GmbH, Austria; ref (3)) was employed to measure ISOPOOH and MVK + MACR concentrations (cf. SI Appendix §1.1). Intensities are reported herein in normalized count per second (ncps), calculated as the signal of the $C_4H_7O^+$ ion (cps) normalized to the total ion signal of H_3O^+ and $H_5O_2^+$, corrected for transmission. A cold trap was deployed upstream of the PTR-TOF-MS to selectively remove ISOPOOH isomers (4). The approach was to collect data for a period of time with the trap in line followed by a period of time in bypass. A difference signal $\Delta C_4H_7O^+$ measured with and without the trap can be defined (cf. SI Appendix §1.2). Synthesized (1,2)-ISOPOOH was used to perform an on-site calibration of the PTR-TOF-MS for both bypass and trap (cf. SI Appendix §1.3). An on-site MVK standard showed that the sensitivity (ncps ppb^{-1}) of the signal intensity for $C_4H_7O^+$ to the MVK concentration was the same through the bypass as through the trap. Detection limits of ISOPOOH and MVK + MACR were 60 ppt and 8 ppt, respectively for a 1 minute measurement. Uncertainty estimates were based on calibration

with authentic standards and obtained by a Monte Carlo method of sampling from the uncertainties in the $C_4H_7O^+$ signals and calibration parameters (cf. SI Appendix §1.4).

A trap experiment lasted for 15 min, alternating with 15 min in bypass. The first four and the last one of the 1-minute data points in each mode were deleted from the analysis to exclude the transition periods between trap and bypass, resulting in a total of 2810 trap-mode data points for analysis. Of these, 91% of the measurements, which required the presence of an operator for trap maintenance when power failures occurred, were made during daytime (Figure S6).

Atmospheric oxidation of isoprene is most active during the daytime.

Instrumentation for measuring NO, NO_x, and NO_y concentrations was part of the MAOS package. The NO and NO_y data streams were obtained from the ARM data archive (<http://www.arm.gov/campaigns/amf2014goamazon>). NO_x data were not available during IOP1 due to lamp failure of the photolytic converter. The operational detection limits of NO and NO_y were 70 ppt and 100 ppt, respectively. The NO_y concentrations were smoothed by applying a 30-min median filter to minimize the contribution of any local emissions.

1.1. PTR Instrumentation

The PTR-TOF-MS instrument was operated at a drift tube temperature of 80 °C and a drift tube pressure of 220 Pa (2.2 mbar). The drift tube voltage was set to 550 V, resulting in an E/N of 132 Td (E , electric field strength; N , number density of air in the drift tube; unit, Townsend, Td; $1 \text{ Td} = 10^{-21} \text{ V m}^2$).

The inlet system of the PTR-TOF-MS (cf. Figure S7) subsampled from the main trace-gas sampling line. The system had flow lines for calibration and measurement. Three-way valves having contact surfaces of PTFE Teflon (NResearch 225T031) were used to switch between the calibration and measurement modes. The valves were controlled by analog outputs of the PTR-

TOF-MS. Metal-sealed mass flow controllers (MFC; MKS 1479A) without Viton O-rings were used for calibration flow to avoid artifacts of ketone reactions. The inlet system inside the container was maintained above 27 °C to prevent condensation. As a comparison point, the 97.7-percentile of the distribution in dew point temperature of the atmosphere during IOP1 was 26.5 °C.

The instrument background was determined a few times per day using a zero air generator (Parker Balston 75-83NA) in the MAOS container. Laboratory tests prior to deployment indicated that concentrations of target compounds in the outflow of the zero air generator were as low as in ultra-high-purity zero air (Airgas). Instrument sensitivity during IOP1 was determined daily by standard addition (5.14 ppm isoprene and 5.14 ppm MVK in nitrogen; Air Liquide) to ambient air. Background and calibration measurements were carried out at ambient humidity to compensate for possible changes in the instrument response with humidity.

The subsample flow passed either through a cold-trap or along a bypass before being sampled by the PTR-TOF-MS. The trap consisted of a cylindrical glass bottle (ChemGlass CG-1140; 35 × 100 mm) and a 6.4-mm (OD) PFA coil in series, both immersed in a cold bath (Lauda ECO RE 1050) at -40 °C. Compared to the implementation described in *Liu et al.* (4), the inclusion of the glass bottle was new. The glass bottle having a large cross section served to remove much of the water vapor upstream of the PFA Teflon tubing so as to avoid clogging. Ice was removed once per day from the bottle. A constant purge flow of 0.1 sLpm through the trap was maintained during bypass to reduce the equilibration time for switching from bypass to trap measurement.

PTR-TOF-MS spectra were collected at a time resolution of 60 s using Tof-DAQ recorder (v. 1.2.92; TOFWERKS). Analog outputs of the PTR-TOF-MS (i.e., determining valve status) were recorded simultaneously. The Tof-DAQ recorder was set to perform automatic mass calibrations every 6 min using peaks at m/z 39.0327 ($\text{H}_5\text{O}(^{18}\text{O})^+$), m/z 59.0491 ($\text{C}_3\text{H}_7\text{O}^+$), and m/z 123.9454 (FeH_4O_4^+). Time series of integrated ion signals for isoprene (C_5H_9^+ ; m/z 69.0699) and MVK/MACR/ISOPOOH ($\text{C}_4\text{H}_7\text{O}^+$; m/z 71.0492) in counts per second (cps) were generated using the Tof-DAQ viewer software (v 1.2.92 TOFWERK, Switzerland).

1.2. Determination and compound assignment of $\Delta\text{C}_4\text{H}_7\text{O}^+$

The bypass intensities at the time points of the trap measurements were obtained by applying linear interpolation and low-pass filtering to the bypass measurements before and after each trap experiment. Figure S8 shows the interpolated bypass signals of $\text{C}_4\text{H}_7\text{O}^+$ and the signal difference $\Delta\text{C}_4\text{H}_7\text{O}^+$ on March 14 and 30, 2014. Interpolation of the bypass signals to the times of the trap measurements can introduce some error in the signal difference, particularly when concentrations are changing rapidly with time, resulting in a large variance in $\Delta\text{C}_4\text{H}_7\text{O}^+$. A histogram of all the $\Delta\text{C}_4\text{H}_7\text{O}^+$ values is shown in Figure S9. Despite the large variance in the $\Delta\text{C}_4\text{H}_7\text{O}^+$ data, the median value is significantly greater than zero, indicating net removal of low-volatility compounds by the trap.

The possibility of significant contributions to $\Delta\text{C}_4\text{H}_7\text{O}^+$ by compounds other than ISOPOOH was considered. Pinonaldehyde ($\text{C}_{10}\text{H}_{16}\text{O}_2$) and isoprene epoxydiols (IEPOX; $\text{C}_5\text{H}_{10}\text{O}_3$) fragment to the $\text{C}_4\text{H}_7\text{O}^+$ ion and can be removed at low temperature (5). Nevertheless, for the study conditions the following lines of evidence appear to rule out these species as substantial contributors to the observed $\Delta\text{C}_4\text{H}_7\text{O}^+$ values. For pinonaldehyde, $\text{C}_4\text{H}_7\text{O}^+$ is a minor fragment ion, and its intensity is about one third of the major fragment ion $\text{C}_{10}\text{H}_{15}\text{O}^+$ (6). The

observed intensity of $C_{10}H_{15}O^+$ ion was less than 15% of $\Delta C_4H_7O^+$ under background conditions, suggesting that the possible contribution of pinonaldehyde to $\Delta C_4H_7O^+$ was less than 5%. Additional evidence is that the concentration of pinonaldehyde, represented by the signal intensity of $C_{10}H_{15}O^+$, did not increase during times of background conditions. The other possibility, IEPOX compounds, was evaluated by sampling authentic IEPOX standards. The results show that the $C_4H_7O^+$ ion was a minor fragment for the standards, corresponding to less than 10% of the main product ion ($C_5H_7O^+$), at least for the employed PTR-TOF-MS operating conditions. Based on the signal intensity of $C_5H_7O^+$ observed for background air masses and changes with the trap in place, the IEPOX contribution accounted for no more than 5% of the observed $\Delta C_4H_7O^+$.

1.3. Calibration using authentic ISOPOOH compounds

(1,2)-ISOPOOH was synthesized (7) and used to perform an RH-dependent calibration at T3 of the PTR-TOF-MS for both bypass and trap modes. Further calibration was undertaken later in the laboratory using both (1,2)-ISOPOOH and (4,3)-ISOPOOH standards. For calibration at T3, (1,2)-ISOPOOH was synthesized at laboratories in Manaus, and analytical tools were not available to determine purity. The purity was inferred based on the instrument response of (1,2)-ISOPOOH later characterized in the laboratory (vide infra). For calibration, the (1,2)-ISOPOOH standard was nebulized and flowed into a mixing flask (8). The dilution flow to the mixing flask was humidified to controlled RH values using a bubbler.

For bypass mode, laboratory experiments using standards of known purity suggested that the conversion efficiency of (1,2)-ISOPOOH to MVK in PTR-ToF-MS was close to unity. The measured sensitivity $\Gamma_{C_4H_7O^+, ISOPOOH}$ of (1,2)-ISOPOOH at $C_4H_7O^+$ was $(95 \pm 5)\%$ of the sensitivity $\Gamma_{C_4H_7O^+, MVK}$ of MVK. The $C_4H_7O^+$ was the dominant peak on the mass spectra

measured by PTR-ToF-MS for (1,2)-ISOPOOH. In addition, after passing the (1,2)-ISOPOOH-containing flow through a heated stainless steel tube at 80-90 °C to convert (1,2)-ISOPOOH to MVK prior to PTR-MS, the measured signal intensity of $C_4H_7O^+$ ion increased by less than 10%. Experiments using (4,3)-ISOPOOH also suggested almost complete conversion to MACR in PTR-ToF-MS.

Under the assumption that a conversion efficiency of $(95 \pm 5)\%$ from (1,2)-ISOPOOH and (4,3)-ISOPOOH to MVK and MACR can be applied to bypass measurements at T3 site, the inferred purity of (1,2)-ISOPOOH standards synthesized in Manaus (52%) fell in the typical purity range of (1,2)-ISOPOOH standards (50-65%) synthesized using the same method.

For (1,2)-ISOPOOH calibration at trap mode, both lab and field experiments showed that the $C_4H_7O^+$ ion signal did not drop completely to background levels when the trap was in place. Figure a shows the dependence of trap $C_4H_7O^+$ signal on the concentration of ISOPOOH and the humidity of the sample based on on-site calibration using (1,2)-ISOPOOH. At fixed concentration, the trap $C_4H_7O^+$ signal was proportional to humidity. At fixed humidity, the trap signal intensity can be fitted using a second degree polynomial of the concentration. The dependence of trap $C_4H_7O^+$ signal intensity $I_{C_4H_7O^+, ISOPOOH, trap}$ on ISOPOOH concentration and humidity can hence be described using the following equation:

$$I_{C_4H_7O^+, ISOPOOH, trap} = a\Gamma_{C_4H_7O^+, MVK} C_{ISOPOOH} (C_{ISOPOOH} + b)(AH + c), \quad (S1)$$

where $C_{ISOPOOH}$ is the concentration of (1,2)-ISOPOOH in the sample flow in ppb; $\Gamma_{C_4H_7O^+, MVK}$ is the sensitivity of MVK at $C_4H_7O^+$; AH is the absolute humidity of the sample flow in hPa; and a , b , and c are fitting parameters. Figures a and b show the comparison of measured and fitted data of all the calibrations.

The detection of considerable $C_4H_7O^+$ signal for (1,2)-ISOPOOH through the trap suggested that processes other than condensation of ISOPOOH isomers took place in the trap to produce $C_4H_7O^+$ ions. One possibility was that volatile impurities contained in the synthesized standard gave rise to $C_4H_7O^+$ ions. This possibility was not supported, however, by the observation that the $C_4H_7O^+$ signal intensity dropped to close to background level at low humidity and the $C_4H_7O^+$ signal intensity was not linearly proportional to the concentration of (1,2)-ISOPOOH at fixed humidity (Figure b). Another possibility was that (1,2)-ISOPOOH was insufficiently removed by the trap due to competition of the condensation of water vapor. This possibility was excluded based on experiments of increasing the residence time of the calibration flow in the trap, in which case the $C_4H_7O^+$ signal intensity slightly increased instead of decreased.

One plausible possibility is that certain reactions of (1,2)-ISOPOOH in the trap led to MVK. This possibility was consistent with the small increase of trap signal intensity with the increase of residence time (i.e., reaction time). Water vapor or water in another form should be involved in the reaction because the trap $C_4H_7O^+$ signal intensity was proportional to humidity (Figure a). The reactions might have taken place in the upper part of trap, where the temperature transited from ambient of above 27 °C down to -40 °C, and water vapor partly condensed in liquid form. The amount of condensed liquid water should relate to absolute humidity given the temperature gradient. Further studies are needed to understand the reaction mechanism, the role of water, and possible designs to eliminate the need to use a complex calibration like Eq. (S1).

Figure b shows that at ambient humidity the $C_4H_7O^+$ signal during trap measurements of (1,2)-ISOPOOH was smaller than that of the bypass signal. As a result, through use of Equation S1 the ISOPOOH concentration in the ambient air was obtained based on the difference signal

for $C_4H_7O^+$. The measured signal intensities $I_{C_4H_7O^+, \text{ambient, bypass}}$ of $C_4H_7O^+$ ion when bypassing the cold trap and $I_{C_4H_7O^+, \text{ambient, trap}}$ when passing through the trap are given as follows:

$$I_{C_4H_7O^+, \text{ambient, bypass}} = I_{C_4H_7O^+, \text{bg}} + \Gamma_{C_4H_7O^+, \text{MVK/MACR}} C_{\text{MVK+MACR}} + \Gamma_{C_4H_7O^+, \text{ISOPOOH}} C_{\text{ISOPOOH}}, \quad (\text{S2})$$

$$I_{C_4H_7O^+, \text{ambient, trap}} = I_{C_4H_7O^+, \text{bg}} + \Gamma_{C_4H_7O^+, \text{MVK/MACR}} C_{\text{MVK+MACR}} + I_{C_4H_7O^+, \text{ISOPOOH, trap}}, \quad (\text{S3})$$

where $I_{C_4H_7O^+, \text{bg}}$ is the background signal intensity of $C_4H_7O^+$ ion in ncps; $\Gamma_{C_4H_7O^+, \text{MVK/MACR}}$ is the combined sensitivity of MVK and MACR; $C_{\text{MVK+MACR}}$ is the sum concentration of MVK and MACR; C_{ISOPOOH} is the sum concentration of (1,2)-ISOPOOH and (4,3)-ISOPOOH, both detected as $C_4H_7O^+$ ion in PTR-TOF-MS; $\Gamma_{C_4H_7O^+, \text{ISOPOOH}}$ is the combined sensitivity of (1,2)-ISOPOOH and (4,3)-ISOPOOH; and $I_{C_4H_7O^+, \text{ISOPOOH, trap}}$ is trap signal intensity of the $C_4H_7O^+$ ion as a function of C_{ISOPOOH} and absolute humidity (AH).

For use of Eqs. (S2) and (S3), $I_{C_4H_7O^+, \text{ambient, bypass}}$ and $I_{C_4H_7O^+, \text{ambient, trap}}$ were obtained from ambient measurements. $\Gamma_{C_4H_7O^+, \text{MVK/MACR}}$ and $I_{C_4H_7O^+, \text{bg}}$ were determined by using MVK/MACR standards and pure air generator. For both of the two parameters, there was insignificant difference between trap and bypass measurements. Further studies carried out in laboratory suggested that the bypass sensitivity and the trap response of (4,3)-ISOPOOH were similar with those of (1,2)-ISOPOOH. $\Gamma_{C_4H_7O^+, \text{ISOPOOH}}$ and $I_{C_4H_7O^+, \text{ISOPOOH, trap}}$ were equivalent to those derived for (1,2)-ISOPOOH. By solving Eqs. (S2) and (S3), $C_{\text{MVK+MACR}}$ and C_{ISOPOOH} were determined. More directly, combining Eqs. (S2) and (S3), the signal difference $\Delta C_4H_7O^+$ of bypass and trap measurement is obtained, giving C_{ISOPOOH} in implicit form:

$$\begin{aligned}\Delta C_4H_7O^+ &= I_{C_4H_7O^+, \text{ ambient, bypass}} - I_{C_4H_7O^+, \text{ ambient, trap}} \\ &= 0.95 \Gamma_{C_4H_7O^+, \text{ MVK}} C_{\text{ISOPOOH}} - a \Gamma_{C_4H_7O^+, \text{ MVK}} C_{\text{ISOPOOH}} (C_{\text{ISOPOOH}} + b)(AH + c).\end{aligned}\quad (\text{S4})$$

1.4. Uncertainty estimate of the ISOPOOH concentration and concentration ratio ξ

The central value of the concentrations of ISOPOOH and MVK+MACR of each data subset were estimated for the median $\Delta C_4H_7O^+$ and median $I_{C_4H_7O^+, \text{ ambient, trap}}$. The central value of the ratio ξ of concentrations was then determined. Confidence intervals (75%) were obtained by a Monte Carlo method of sampling from the uncertainties in fit parameters in Eq. (S1) (i.e., a , b , and c), the absolute humidity, the bypass sensitivities of ISOPOOH and MVK at $C_4H_7O^+$, the median $\Delta C_4H_7O^+$, and the median $I_{C_4H_7O^+, \text{ ambient, trap}}$.

2. Modeling

Three models were used to aid in the interpretation of the measurements. (1) An analytical model was used to infer production ratio χ from observed concentration ratio ξ . Details of this model are presented in the main text and in SI Appendix §2.1. (2) A measurement-constrained box model of the chemistry in the planetary boundary layer was used to simulate daytime HO_2 and RO_2 concentrations for variable NO concentration (1 to 400 ppt). The model was used to determine the corresponding fractional loss of ISOPOO via each reaction pathway and hence the production ratio χ . (3) Simulation results using GEOS-Chem, a global three-dimensional chemical transport model, were compared with observations.

For the box model, the chemistry component consisted of the Master Chemical Mechanism (MCM; version 3.3.1; ref (9)). In addition, some recent experimental results on the chemical production and fate of MVK, MACR, and ISOPOOH were incorporated (4, 10). A basic representation of deposition and entrainment was implemented (cf. SI Appendix §2.2). The model was configured to simulate daytime chemistry (10:00-17:00 local time (LT); 14:00-21:00

UTC). Most trap measurements were made during this time period (Figure S6), and the concentrations of isoprene and its oxidation products were relatively stable (Figure S3). Irradiance levels were held constant, corresponding to the solar zenith angle at 14:30 LT, with no diel cycle for photolysis (cf. SI Appendix §2.3). The temperature was set at 298 K. The simulation was constrained by constant concentrations of isoprene (1.7 ppb), monoterpenes (0.17 ppb), methane (1.85 ppm), and carbon monoxide (110 ppb) at the observed daytime mean values. The hydroxyl radical concentration was fixed at $5 \times 10^5 \text{ cm}^{-3}$. The concentrations of HO_2 and RO_2 (cf. SI Appendix §2.4), fractional loss of ISOPOO by reaction with NO, HO_2 , RO_2 , and isomerization (cf. main text), and production ratio χ (cf. main text) were obtained at steady state.

For the CTM, the simulations were run in GEOS-Chem (11) for the year 2012 on a $4^\circ \times 5^\circ$ grid with a model spin-up of 1.5 years. The GEOS5 meteorology and the Rosenbrock Rodas-3 solver was used. The chemical mechanism was largely as described in reference (12) but included several updates of the isoprene chemistry based on recent laboratory results (10, 13-16). Information obtained from the simulations included the daytime average values of the concentration ratio ζ , the NO concentration, the NO_y concentration, and the fractional loss of ISOPOO radicals to individual pathways. This information was obtained for February and March over the grid box encompassing the observation site (<1000 m height). In addition to the simulation using default settings, simulations that increased above-canopy NO emissions by factors of 10 and 30 were carried out. Further information is provided in SI Appendix §2.5.

2.1. Analytical model to estimate of χ from ζ

The time course of concentration C_i of species i , where i is one of (1,2)-ISOPOOH, (4,3)-ISOPOOH, MVK, or MACR, is governed by the following equation:

$$\frac{dC_i}{dt} = S_i - k_i C_i, \quad (\text{S5})$$

where S_i is the production rate via the reaction of isoprene with OH and k_i is the first-order loss coefficient. For constant S_i and k_i , the solution to Eq. (S5) is as follows:

$$C_i(t) = \frac{S_i}{k_i} (1 - e^{-k_i t}) + C_i(0) e^{-k_i t}, \quad (\text{S6})$$

Before sunrise (i.e., taken as time zero), the concentrations of MVK, MACR, and ISOPOOH approach zero (cf. Figure S3). For $C_i(0) = 0$, the following equation is obtained:

$$\begin{aligned} \xi &= \frac{C_{\text{ISOPOOH}}}{C_{\text{MVK+MACR}}} = \frac{\frac{S_1}{k_1} (1 - e^{-k_1 t}) + \frac{S_2}{k_2} (1 - e^{-k_2 t})}{\frac{S_3}{k_3} (1 - e^{-k_3 t}) + \frac{S_4}{k_4} (1 - e^{-k_4 t})} \\ &= \frac{\frac{f_{1+2}^1 S_{1+2}}{k_1} (1 - e^{-k_1 t}) + \frac{f_{1+2}^2 S_{1+2}}{k_2} (1 - e^{-k_2 t})}{\frac{f_{3+4}^3 S_{3+4}}{k_3} (1 - e^{-k_3 t}) + \frac{f_{3+4}^4 S_{3+4}}{k_4} (1 - e^{-k_4 t})}, \quad (\text{S7}) \\ &= \frac{(0.6/k_1) (1 - e^{-k_1 t}) + (0.4/k_2) (1 - e^{-k_2 t})}{(0.6/k_3) (1 - e^{-k_3 t}) + (0.4/k_4) (1 - e^{-k_4 t})} \chi \end{aligned}$$

where the indices 1-4 represent (1,2)-ISOPOOH, (4,3)-ISOPOOH, MVK, and MACR, respectively; f_{1+2}^1 , f_{1+2}^2 , f_{3+4}^3 , and f_{3+4}^4 are the respective fractions of the total production rates S_{1+2} and S_{3+4} (e.g., $S_{1+2} = S_1 + S_2$ and $f_{1+2}^1 = S_1/S_{1+2}$); and $\chi = S_{1+2}/S_{3+4}$. The fractions f_{1+2}^1 , f_{1+2}^2 , f_{3+4}^3 , and f_{3+4}^4 are independent of S_{1+2} and S_{3+4} and are ultimately determined by the branching ratio of isoprene to the respective precursor peroxy radicals. MVK and (1,2)-ISOPOOH originate from the same isoprene peroxy radical. MACR and (4,3)-ISOPOOH likewise originate from the same radical. Values $f_{1+2}^1 = f_{3+4}^3 = 0.6$ and $f_{1+2}^2 = f_{3+4}^4 = 0.4$ are used based on the reported ratio of

product yields of MVK and MACR via the NO pathway (4). For a given reaction time, χ is directly proportional to ζ .

Loss coefficients k_i of MVK, MACR, and ISOPOOH and an effective reaction time are needed in order to calculate the proportionality coefficient of χ to ζ using Eq. (S7). The loss coefficient is given by $k_i = k_{i,\text{OH}}[\text{OH}] + k_{i,\text{en}} + k_{i,\text{d}}$ for rate coefficients of reaction (OH), entrainment (*en*), and deposition (*d*). Parameter values are listed in Table S1. The entrainment process of these species is less well understood compared to deposition as well to OH oxidation. The sensitivity of the proportionality coefficient χ/ζ to k_{en} is investigated. Values of k_{en} used for the sensitivity study are 0, 1, and $2 \times 10^5 \text{ s}^{-1}$, where $1 \times 10^5 \text{ s}^{-1}$ is the best estimate based on current knowledge (cf. Table S1). As shown in Figure S11, the proportionality factor for an effective reaction time of 5 h changed by less than 2% for a change in the entrainment coefficient from $1 \times 10^5 \text{ s}^{-1}$ to 0 or $2 \times 10^5 \text{ s}^{-1}$. The production ratio χ inferred from the concentration ratio ζ is therefore considered insensitive to the coefficient k_{en} of entrainment.

Plots of Eq. (S7) in Figure S4 show the dependence of χ on ζ for different reaction times ranging from 0 to 10 h. Figure S4 is drawn for an average daytime OH concentration of $5 \times 10^5 \text{ cm}^{-3}$ for background conditions (17). The proportionality coefficient relating χ to ζ was greater than unity for any reaction time t because of the longer lifetimes of MVK and MACR compared to those of (1,2)-ISOPOOH and (4,3)-ISOPOOH. The proportionality coefficient increases for greater reaction times. For an assumed effective reaction time of 5 h representing daybreak to midafternoon (green line, Figure S4), the slope is 1.5. The confidence interval of 0.4 to 0.6 for ζ under background conditions (cf. Figure 2b in the main text) implies a range of 0.6 to 0.9 for χ .

As a test of the accuracy of the effective photochemical reaction time (i.e., $5 \times 10^5 \text{ OH cm}^{-3}$ across 5 h), the ratio $C_{\text{total}}/C_{\text{ISOP}}$ of the total concentration of measured reaction products

(i.e., the sum of MVK, MACR, and ISOPOOH) to the isoprene concentration was calculated using the following equation:

$$\begin{aligned}
C_{\text{total}}/C_{\text{ISOP}} &= \frac{S_{\text{total}}}{C_{\text{ISOP}}} \cdot \left\{ \frac{0.6}{k_1} \frac{\chi}{1+\chi} \left(1 - e^{-k_1 t_{\text{eff}}}\right) + \frac{0.4}{k_2} \frac{\chi}{1+\chi} \left(1 - e^{-k_2 t_{\text{eff}}}\right) \right. \\
&\quad \left. + \frac{0.6}{k_3} \frac{1}{1+\chi} \left(1 - e^{-k_3 t_{\text{eff}}}\right) + \frac{0.4}{k_4} \frac{1}{1+\chi} \left(1 - e^{-k_4 t_{\text{eff}}}\right) \right\}, \quad (\text{S8}) \\
&= 0.65 k_{\text{ISOP,OH}} [\text{OH}] \cdot \left\{ \frac{0.6}{k_1} \frac{\chi}{1+\chi} \left(1 - e^{-k_1 t_{\text{eff}}}\right) + \frac{0.4}{k_2} \frac{\chi}{1+\chi} \left(1 - e^{-k_2 t_{\text{eff}}}\right) \right. \\
&\quad \left. + \frac{0.6}{k_3} \frac{1}{1+\chi} \left(1 - e^{-k_3 t_{\text{eff}}}\right) + \frac{0.4}{k_4} \frac{1}{1+\chi} \left(1 - e^{-k_4 t_{\text{eff}}}\right) \right\}
\end{aligned}$$

where the variables k_i and χ are the same as in Eq. (S7) and S_{total} is the total production rate of MVK, MACR, and ISOPOOH. The term S_{total} is equal to $0.65 k_{\text{ISOP,OH}} C_{\text{ISOP}} [\text{OH}]$ based on MCM v3.3.1 for background conditions. Other values include $t_{\text{eff}} = 5$ h and $[\text{OH}] = 5 \times 10^5 \text{ cm}^{-3}$. For χ ranging from 0.61 to 0.93 for background conditions, the calculated $C_{\text{total}}/C_{\text{ISOP}}$ ranges from 0.41 to 0.43. This value is in good agreement with the median of the observations of 0.4 for background condition, as illustrated in Fig. S2.

One approximation of the foregoing analysis is the use of production rates S_i and loss coefficients k_i that are constant throughout the day, thereby corresponding to average or effective daily values. One critical simplification in this treatment is the entrainment processes. Whereas it is reasonable to assume that cleaner air is entrained from upper troposphere into the boundary layer for afternoon hours, entrainment of air from the residual layer, which might contain some MVK and MACR due to their longer lifetime, can occur in the morning. In this case, entrainment in the morning can be a source or neutral instead of a sink. Possible entrainment from the residual layer to the boundary layer in the morning can be viewed as a small but nonzero initial concentration of MVK and MACR in the model. In this case, concentration ratio $\zeta(t)$ can be

calculated given production ratio χ and $C_{\text{MVK+MACR}}(0)$, but χ cannot be retrieved just based on $\zeta(t)$. As a sensitivity test on $C_{\text{MVK+MACR}}(0)$, $\zeta(t)$ is plotted for $C_{\text{MVK+MACR}}(0) = 0$ and 0.1 ppb in Figure S12. The value of χ is fixed at 0.75, which is the estimated median value for the background condition (cf. Figure S4). For $t < 2$ h, the concentration ratio ζ varies strongly with $C_{\text{MVK+MACR}}(0)$. As t increases, $\zeta(t)$ for different $C_{\text{MVK+MACR}}(0)$ converge. For an effective reaction time of 5 h, ζ values for $C_{\text{MVK+MACR}}(0)$ of 0.1 ppb is 12% lower than that for $C_{\text{MVK+MACR}}(0)$ of 0 ppb. The conclusion is that the afternoon concentration ratio ζ is not sensitive to possible morning entrainment of MVK and MACR from residual layer, and the simplified treatment of entrainment used here is acceptable.

2.2. Box model: Deposition and entrainment

Deposition and entrainment rate coefficients of ISOPOOH, MVK, and MACR are set as the same values as in the analytical model (cf. Table S1). In addition, deposition of O_3 , H_2O_2 , HNO_3 , and PAN was also considered, with deposition velocities of 1, 5, 3, 2 cm s^{-1} , respectively (13, 18). The effective entrainment loss coefficient of $1.0 \times 10^{-5} \text{ s}^{-1}$ for MVK, MACR, and ISOPOOH (cf. Table S1) was also applied to all the other oxygenated oxidation products.

2.3. Box model: Photolysis

The parameterization for photolysis frequencies in Master Chemical Mechanism (MCM) was historically calibrated for clear sky condition using a radiation transfer model (19). The parameterization (photolysis frequency as a function of solar zenith angle) represents clear sky conditions at a latitude of 45 °N at summertime (20). Site T3 was located near the equator with a different column air mass. For inorganics included in MCM, the noon-time photolysis frequencies at T3 site calculated using the MCM parameterization were on average 18% lower than those simulated by us in a test using the Tropospheric Ultraviolet and Visible (TUV) model

(<https://www2.acom.ucar.edu/modeling/tropospheric-ultraviolet-and-visible-tuv-radiation-model>). A scaling factor of 1.2 was, therefore, applied in the model treatment herein to the photolysis frequencies simulated by MCM for clear sky conditions. A further factor was incorporated for all sky conditions. A sky radiometer at T3 measured the shortwave broadband total downwelling irradiance (SKYRAD). For the days and hours of trap measurements, the average irradiance level for all skies was estimated as 76% of clear skies. Scaling factors of 1.2 and 0.76 represented a net 0.91 factor applied to the MCM photolysis frequencies for the modeling activities carried out in the present study.

2.4. Box model: Simulated HO₂ and RO₂ concentrations

The simulated HO₂ and RO₂ concentrations using the box model are in the range of measurement values for in tropical forests, as reported in the literature, both in terms of magnitude and ratio. Lelieveld et al. (21) reported a mean HO₂ concentration of $(11 \pm 3) \times 10^8$ cm⁻³ for a mean NO concentration of 0.02 ± 0.02 ppb over coastal Amazonia during the GABRIEL aircraft campaign. The HO₂ measurement technique was later found to have a significant interference from RO₂ radicals produced from OH reaction with alkene- and aromatic-precursors including isoprene, which contribute to the nominal detection of HO₂ radicals by a conversion efficiency of greater than 80% (22). As shown in Figure S13, although the simulated HO₂ concentration is below 4×10^8 cm⁻³, the total concentration of HO₂ and RO₂ is 8×10^8 cm⁻³ for 0.02 ppb NO. This simulated range is close to the observation of Lelieveld et al. (21) with correction for the measurement interference. Observations over southeast Asia in the OP3 Experiment found a mean mid-day total concentration of HO₂ and RO₂ of $(9 \pm 2) \times 10^8$ cm⁻³ for a mean NO concentration of 0.04 ppb (23). By comparison, in the present study, the simulated concentration of HO₂ + RO₂ is 7×10^8 cm⁻³ for 0.04 ppb NO. As shown in Figure S13,

the simulated concentration of RO₂ is several times higher than that of HO₂ at lower NO concentrations. The HO₂ and RO₂ become similar at higher NO concentrations. This trend is quantitatively consistent with the field observations by Fleming et al. (24). In that study, the fraction of HO₂ in the total concentration of HO₂ and RO₂ was 0.2 for lower NO_x and 0.4 to 0.6 for higher NO_x. Although the concentrations of HO₂ and RO₂ are often assumed to be equal (25), the simulation here as well as the cited observations suggest that the concentration ratio of HO₂ to RO₂ decreases below unity for low NO concentration.

2.5. GEOS-Chem Simulation: Sensitivity to soil NO emissions

There have been only a few field studies of soil NO emission in the Amazon rainforests in the wet season (26-28). The reported soil NO emission rates are in the range of 0.6 to 1.4×10^{10} molec cm⁻² s⁻¹. For dry season, the reported soil NO emission can be higher (27-29). One must keep in mind the wide range of soils and forest types throughout Amazonia, so that these measurements reported in the literature cannot be readily generalized; even so, they are the measurements that we do have at this time, and they do represent what models are based on. Furthermore, not all the NO emitted from forest soil is exported to the atmosphere above the canopy due to NO oxidation by ozone forming NO₂ and subsequent NO₂ deposition within the canopy. There is large uncertainty in the canopy reduction factor, defined as the ratio of above-canopy NO_x emission to above-soil NO emission (30). For tropical forests, earlier study by Jacob and Bakwin suggested a canopy reduction factor of around 0.2 (31), whereas later study by Ganzeveld et al. (30) suggested a value of 0.4-0.5. Based on these studies, the above-canopy NO_x emission can be in the range of 1.2 to 7.0×10^9 molec cm⁻² s⁻¹.

Soil NO emission in GEOS-Chem is based on parameterization by Hudman et al. (32), and canopy reduction is implemented following Jacob and Bakwin (31) (cf.

http://wiki.seas.harvard.edu/geos-chem/index.php/Hudman_et_al_2012_soil_NOx_emissions_algorithm). For the grid square encompassing the measurement site, the modeled above-canopy NO_x emission is 2.0×10^8 molec cm⁻² s⁻¹ in the wet season. The value is one order of magnitude lower than the range suggested by the field observations. In this light, we reran the model with increased soil NO emissions by factors of 10 and 30 and kept the canopy reduction unchanged. The simulation results are presented in Table S4. The resultant above-canopy NO_x emissions are 2.0 to 6.0×10^9 molec cm⁻² s⁻¹, respectively. The modeled daytime ratio of ISOPOOH concentration to MVK + MACR concentration is 1.0, 0.93, and 0.76 for default, $10 \times$ default, and $30 \times$ default soil NO emission scenarios, respectively, in the wet season in the grid square where measurement site is located. The simulated concentration ratios with increased NO_x emissions, especially in the case of NO emission that are 30 times higher, get closer to the confidence interval of the observed ratio of 0.4-0.6 reported in the present study.

References

1. Martin ST, *et al.* (2015) Introduction: Observations and Modeling of the Green Ocean Amazon (GoAmazon2014/5). *Atmos. Chem. Phys. Discuss.* 15(21):30175-30210.
2. Guenther A, *et al.* (2006) Estimates of global terrestrial isoprene emissions using MEGAN (Model of Emissions of Gases and Aerosols from Nature). *Atmos. Chem. Phys.* 6(11):3181-3210.
3. Jordan A, *et al.* (2009) An online ultra-high sensitivity proton-transfer-reaction mass-spectrometer combined with switchable reagent ion capability (PTR+SRI-MS). *Int. J. Mass. Spectrom.* 286(1):32-38.
4. Liu YJ, Herdinger-Blatt I, McKinney KA, & Martin ST (2013) Production of methyl vinyl ketone and methacrolein via the hydroperoxyl pathway of isoprene oxidation. *Atmos. Chem. Phys.* 13(11):5715-5730.
5. Nguyen TB, *et al.* (2014) Overview of the Focused Isoprene eXperiment at the California Institute of Technology (FIXCIT): mechanistic chamber studies on the oxidation of biogenic compounds. *Atmos. Chem. Phys.* 14(24):13531-13549.
6. Wisthaler A, Jensen NR, Winterhalter R, Lindinger W, & Hjorth J (2001) Measurements of acetone and other gas phase product yields from the OH-initiated oxidation of terpenes by proton-transfer-reaction mass spectrometry (PTR-MS). *Atmos. Environ.* 35(35):6181-6191.

7. Rivera-Rios JC, *et al.* (2014) Conversion of hydroperoxides to carbonyls in field and laboratory instrumentation: observational bias in diagnosing pristine versus anthropogenically-controlled atmospheric chemistry. *Geophys. Res. Lett.* 41(23):8645-8651.
8. Liu YJ, *et al.* (2015) Uptake of epoxydiol isomers accounts for half of the particle-phase material produced from isoprene photooxidation via the HO₂ pathway. *Environ. Sci. Technol.* 49(1):250-258.
9. Jenkin ME, Young JC, & Rickard AR (2015) The MCM v3.3.1 degradation scheme for isoprene. *Atmos. Chem. Phys.* 15(20):11433-11459.
10. St. Clair JM, *et al.* (2016) Kinetics and products of the reaction of the first-generation isoprene hydroxy hydroperoxide (ISOPOOH) with OH. *J. Phys. Chem. A* 120(9):1441-1451.
11. Bey I, *et al.* (2001) Global modeling of tropospheric chemistry with assimilated meteorology: Model description and evaluation. *J. Geophys. Res.-Atmos.* 106(D19):23073-23095.
12. Mao J, *et al.* (2013) Ozone and organic nitrates over the eastern United States: Sensitivity to isoprene chemistry. *J. Geophys. Res.-Atmos.* 118(19):11256-11268.
13. Nguyen TB, *et al.* (2015) Rapid deposition of oxidized biogenic compounds to a temperate forest. *P. Natl. Acad. Sci. USA* 112(5):E392-E401.
14. Bates KH, *et al.* (2014) Gas phase production and loss of isoprene epoxydiols. *J. Phys. Chem. A* 118(7):1237-1246.
15. Praske E, *et al.* (2015) Atmospheric fate of methyl vinyl ketone: peroxy radical reactions with NO and HO₂. *J. Phys. Chem. A* 119(19):4562-4572.
16. Bates KH, *et al.* (2016) Production and fate of C₄ dihydroxycarbonyl compounds from isoprene oxidation. *J. Phys. Chem. A* 120(1):106-117.
17. Kim S, *et al.* (2013) Evaluation of HO_x sources and cycling using measurement-constrained model calculations in a 2-methyl-3-butene-2-ol (MBO) and monoterpene (MT) dominated ecosystem. *Atmos. Chem. Phys.* 13(4):2031-2044.
18. Fan S-M, Wofsy SC, Bakwin PS, Jacob DJ, & Fitzjarrald DR (1990) Atmosphere-biosphere exchange of CO₂ and O₃ in the central Amazon Forest. *J. Geophys. Res.-Atmos.* 95(D10):16851-16864.
19. Jenkin ME, Saunders SM, & Pilling MJ (1997) The tropospheric degradation of volatile organic compounds: A protocol for mechanism development. *Atmos. Environ.* 31(1):81-104.
20. Saunders SM, Jenkin ME, Derwent RG, & Pilling MJ (2003) Protocol for the development of the Master Chemical Mechanism, MCM v3 (Part A): tropospheric degradation of non-aromatic volatile organic compounds. *Atmos. Chem. Phys.* 3(1):161-180.
21. Lelieveld J, *et al.* (2008) Atmospheric oxidation capacity sustained by a tropical forest. *Nature* 452(7188):737-740.
22. Fuchs H, *et al.* (2011) Detection of HO₂ by laser-induced fluorescence: calibration and interferences from RO₂ radicals. *Atmos. Meas. Tech.* 4(6):1209-1225.
23. Hewitt CN, *et al.* (2010) Overview: oxidant and particle photochemical processes above a south-east Asian tropical rainforest (the OP3 project): introduction, rationale, location characteristics and tools. *Atmos. Chem. Phys.* 10(1):169-199.

24. Fleming ZL, *et al.* (2006) Peroxy radical chemistry and the control of ozone photochemistry at Mace Head, Ireland during the summer of 2002. *Atmos. Chem. Phys.* 6(8):2193-2214.
25. Barkot DJ, Jr., *et al.* (2004) A study of the NO_x dependence of isoprene oxidation. *J. Geophys. Res.* 109(D11):D11310.
26. Bakwin PS, *et al.* (1990) Emission of nitric oxide (NO) from tropical forest soils and exchange of NO between the forest canopy and atmospheric boundary layers. *J. Geophys. Res.-Atmos.* 95(D10):16755-16764.
27. Verchot LV, *et al.* (1999) Land use change and biogeochemical controls of nitrogen oxide emissions from soils in eastern Amazonia. *Global Biogeochem. Cycles* 13(1):31-46.
28. Garcia-Montiel DC, *et al.* (2001) Controls on soil nitrogen oxide emissions from forest and pastures in the Brazilian Amazon. *Global Biogeochem. Cycles* 15(4):1021-1030.
29. Kaplan WA, Wofsy SC, Keller M, & Da Costa JM (1988) Emission of NO and deposition of O₃ in a tropical forest system. *J. Geophys. Res.-Atmos.* 93(D2):1389-1395.
30. Ganzeveld LN, *et al.* (2002) Global soil-biogenic NO_x emissions and the role of canopy processes. *J. Geophys. Res.-Atmos.* 107(D16):ACH 9.
31. Jacob DJ & Bakwin PS (1991) Cycling of NO_x in tropical forest canopies. *Microbial production and consumption of greenhouse gases: methane, nitrogen oxides, and halomethanes*, eds Rogers JE & Whitman WB (American Society for Microbiology, Washington, D.C.), pp 237-253.
32. Hudman RC, *et al.* (2012) Steps towards a mechanistic model of global soil nitric oxide emissions: implementation and space based-constraints. *Atmos. Chem. Phys.* 12(16):7779-7795.
33. Atkinson R, *et al.* (2006) Evaluated kinetic and photochemical data for atmospheric chemistry: Volume II - gas phase reactions of organic species. *Atmos. Chem. Phys.* 6(11):3625-4055.
34. Vilà-Guerau de Arellano J, van den Dries K, & Pino D (2009) On inferring isoprene emission surface flux from atmospheric boundary layer concentration measurements. *Atmos. Chem. Phys.* 9(11):3629-3640.
35. Kuhn U, *et al.* (2007) Isoprene and monoterpene fluxes from Central Amazonian rainforest inferred from tower-based and airborne measurements, and implications on the atmospheric chemistry and the local carbon budget. *Atmos. Chem. Phys.* 7(11):2855-2879.
36. Karl T, *et al.* (2007) The tropical forest and fire emissions experiment: Emission, chemistry, and transport of biogenic volatile organic compounds in the lower atmosphere over Amazonia. *J. Geophys. Res.-Atmos.* 112(D18):D18302.
37. Peeters J, Müller J-F, Stavrou T, & Nguyen VS (2014) Hydroxyl radical recycling in isoprene oxidation driven by hydrogen bonding and hydrogen tunneling: The upgraded LIM1 mechanism. *J. Phys. Chem. A* 118(38):8625-8643.

List of Tables

Table S1. Loss rate coefficients for species in Eq. (1) for background conditions. A 1000-m deep, well mixed planetary boundary layer (PBL) is assumed. A temperature of 298 K is used.

Species, <i>i</i>	$k_{i,\text{OH}} (10^{-5} \text{ s}^{-1})$ ^a	$k_{i,\text{d}} (10^{-5} \text{ s}^{-1})$ ^b	$k_{i,\text{en}} (10^{-5} \text{ s}^{-1})$ ^c	$k_i (10^{-5} \text{ s}^{-1})$ ^d
(1,2)-ISOPOOH	3.7	2.0	1.0	6.7
(4,3)-ISOPOOH	5.9	2.0	1.0	8.9
MVK	1.0	0.2	1.0	2.2
MACR	1.4	0.2	1.0	2.6

- ^(a) For reactions with OH, the rate coefficients were taken from IUPAC recommendation for MVK and MACR (33) and from St. Clair et al. for (1,2)-ISOPOOH and (4,3)-ISOPOOH (10). A daytime (10:00-17:00 LT) background OH concentration of $5 \times 10^5 \text{ cm}^{-3}$ was used, as measured by a chemical ionization mass spectrometer at T3 (17). These values hold for background conditions. Oxidation can be faster inside the pollution plume.
- ^(b) A deposition velocity of 2.0 cm s^{-1} was used for ISOPOOH isomers, as recommended recently by Nguyen et al. (13) based on measurements over a temperate forest. For MVK and MACR, the deposition rate was assumed to be one magnitude lower (i.e., 0.2 cm s^{-1}) considering its lower water solubility and reactivity.
- ^(c) An entrainment rate coefficient was determined by considering the entrainment velocity and concentration gradient between PBL and cloud layer. An entrainment velocity of 2.0 cm s^{-1} was taken based on the simulated evolution of PBL height over a tropical forest during daytime (10:00-17:00 LT) (34). Based on reported vertical profiles of isoprene concentration and the ratio of the concentration of (MVK+MACR+ISOPOOH) to that of isoprene over central Amazonia (35, 36), the concentration jump of MVK, MACR, and ISOPOOH between the PBL and the cloud layer is approximated by half of PBL concentration. Compared with a concentration jump of isoprene of one order of magnitude, the concentration jump of MVK, MACR, and ISOPOOH is smaller because of enhanced oxidation in the cloud layer (35, 36). The uncertainty of the current parameterization of entrainment rate can be a factor of two due to limited understanding of entrainment processes of these species. Sensitivity of model results to entrainment rate was examined (cf. SI §2.1).
- ^(d) The first-order loss coefficient is given by $k_i = k_{i,\text{OH}}[\text{OH}] + k_{i,\text{en}} + k_{i,\text{d}}$.

Table S2. Reported production yields of MVK+MACR and ISOPOOH via individual pathways.^a

	$Y_{\text{MVK+MACR}}$	Y_{ISOPOOH}
HO ₂ Pathway	6.3% (4)	90% (10)
NO Pathway	71% (4)	0
RO ₂ Pathway	75% ^b	0
ISOM Pathway	10% ^c	0

^(a) For measurement-based values, the reference is included in the parentheses.

^(b) Although the MVK and MACR yields were reported for several “low-NO” experiments, the contribution of RO₂ pathway is not clear. The value adopted here is based on MCM v3.1.1 (9).

^(c) Theoretical prediction by Peeters et al. (37). There is no direct laboratory evidence that MVK and MACR can be produced via the isomerization pathway.

Table S3. Simulation results using a box model with different chemical mechanisms.^a

	MCM 3.3.1 + updates ^{b,c}	MCM 3.3.1	MCM 3.2 + updates ^{c,d}	MCM 3.2
NO (ppt)	16-30	19-33	19-36	22-40
f_{HO_2}	0.31-0.39	0.29-0.36	0.39-0.51	0.37-0.48
f_{NO}	0.27-0.40	0.30-0.42	0.40-0.55	0.44-0.58
f_{RO_2}	0.03-0.05	0.03-0.04	0.05-0.09	0.05-0.08
f_{ISOM}	0.25-0.30	0.26-0.30	0	0
$f_{\text{HO}_2}: f_{\text{NO}}$	0.8-1.4	0.7-1.2	0.7-1.3	0.6-1.1

^(a) Inferred range of NO concentrations and fractional contribution to ISOPOO reaction from observation-constraint χ range of 0.61-0.93 using four sets of chemical mechanisms.

^(b) Mechanism used in the main text (Figure 3 in main text).

^(c) Updates include measured production yields of MVK and MACR via the HO₂ pathway (4) and measured reaction rate coefficients of (1,2)-ISOPOOH and (4,3)-ISOPOOH with OH (10).

^(d) Compared with MCM 3.3.1, MCM 3.2 does not include isomerization pathway of ISOPOO reaction.

Table S4. Simulation results using GEOS-Chem for central Amazonia.^a

<i>Model settings</i>			
Soil NO _x emission ^b	default	default × 10	default × 30
<i>Simulation results</i>			
Above-canopy NO _x emissions (molec m ⁻² s ⁻¹)	2.0 × 10 ⁸	2.0 × 10 ⁹	6.0 × 10 ⁹
Daytime NO concentration (ppt)	7.5	10	15
Daytime NO _y concentration (ppb)	0.11	0.18	0.36
Daytime ISOPOOH concentration (ppb)	0.65	0.62	0.52
Daytime MVK+MACR concentration (ppb)	0.62	0.67	0.68
Concentration ratio ξ	1.0	0.93	0.76
f_{HO_2}	0.59	0.55	0.49
f_{NO}	0.14	0.22	0.34
f_{RO_2}	0.06	0.06	0.05
f_{ISOM}	0.21	0.16	0.13
$f_{\text{HO}_2} : f_{\text{NO}}$	4.3	2.5	1.4

^(a) The simulation results are for the grid square (0° - 4° S, 57.5° - 62.5° W) where the measurement site is located during February and March in 2012.

^(b) Justification of increasing soil NO_x emission by a factor of 10 and 30 is provided in SI §2.5.

List of Figures

Figure S1. Back-trajectories launched at T3 on (a) 14 March 2014 and (b) 30 March 2014. The back-trajectories start at 12 and 18 h (UTC). Colors differentiate back-trajectories launched at height 660 m (orange), 270 m (white) and 90 m (cyan).

Figure S2. Representative afternoon time series (top to bottom) of (1) CO concentrations, O₃ concentrations, OH concentrations, and rain amount, (2) NO_y concentrations and shortwave broadband total downwelling irradiance, (3) wind direction and wind speed, and (4) ratio of total concentration of MVK, MACR and ISOPOOH to isoprene concentration. (a) The left panels of this figure represent polluted conditions (14 March 2014). (b) The right panels represent background conditions (30 March 2014). Local noon is at 16:00 UTC. This figure is a supplement of Figure 1 in the main text.

Figure S3. Diel variation for trap-measurement days of (a) isoprene concentration and (b) the total concentration of MVK, MACR, and ISOPOOH. The solid line and shaded regions respectively represent the median and interquartile ranges of each hour of the day.

Figure S4. Modeled dependence of the production ratio χ on the measured concentration ratio ζ for different reaction times (cf. Eq. (1) in main text). The dashed line projects the central value of ζ measured during background conditions onto the inferred production ratio χ when assuming 5 h of reaction time. The yellow region shows the same when taking into account the confidence interval in ζ . Figure is drawn for 5×10^5 OH cm⁻³, corresponding to daytime background conditions. The black arrow

points to daytime ξ value simulated using a global chemical transport model for this region in a typical wet season.

Figure S5. Histogram of NO concentrations measured by the G1 aircraft in the environs of Manaus during GoAmazon 2014/5. Data are collected at flight heights of 200 to 1000 m. The measured histogram can be fitted as the sum of the histograms under background and polluted conditions, which follow normal and lognormal distribution, respectively. The fitted mean and standard deviation of the normal distribution for background condition is noted in the figure. The large variance of measured NO concentration under background condition (and also the existence of negative values) is largely due to large variation of instrumental background level. The mean value of the normal distribution can represent mean background NO concentration, but its standard deviation can be much larger than the variation of NO concentration.

Figure S6. Histogram of trap measurements in UTC. The yellow region represents local daytime, and the dashed line represents local noon.

Figure S7. Schematic diagram of the gas inlet system for the PTR-TOF-MS. The top and bottom sections represent calibration and measurement set-ups, respectively.

Figure S8. Example time series of (top) $\Delta\text{C}_4\text{H}_7\text{O}^+$ and (btm) $\text{C}_4\text{H}_7\text{O}^+$ signal on (a) 14 March 2014 and (b) 30 March 2014, representing polluted and background conditions, respectively. The black and green points in the bottom panels show the $\text{C}_4\text{H}_7\text{O}^+$ signal intensities measured through the cold trap and along the bypass, respectively. Red lines show the interpolated intensities for the $\text{C}_4\text{H}_7\text{O}^+$ ions measured with the bypass in place.

Figure S9. Histogram of intensity difference $\Delta C_4H_7O^+$, defined as the intensity of the $C_4H_7O^+$ ion signal recorded through compared to in-bypass of the cold trap. The red arrow shows the mean value of $\Delta C_4H_7O^+$.

Figure S10. Calibration curve. (a) Comparison of measured and fitted data in a three-dimensional plot. (b) Comparison and fitting residuals. Point size is scaled by the absolute humidity. The signal intensities of the $C_4H_7O^+$ ion shown in the figures are background-corrected.

Figure S11. The proportionality coefficient, representing by χ/ζ , as a function of reaction time. The loss rate coefficient k_{en} due to entrainment is set to 0, 1, or $2 \times 10^5 \text{ s}^{-1}$.

Figure S12. Ratio ζ of concentrations as a function of reaction time for initial concentration of MVK+MACR of 0 and 0.1 ppb. The production ratio χ was set to 0.75, which is the central value inferred from observations for background condition assuming zero initial concentration of MVK and MACR (cf. Figure S4). The dashed line shows a reaction time of 5 h. The value of ζ is calculated using Eq. (S7) for zero initial concentration and a similar equation for non-zero initial concentration.

Figure S13. Simulated steady-state HO_2 and RO_2 concentrations as a function of NO using the MCM 3.3.1 supplemented with recent experimental results at an OH concentration of $5 \times 10^5 \text{ cm}^{-3}$.

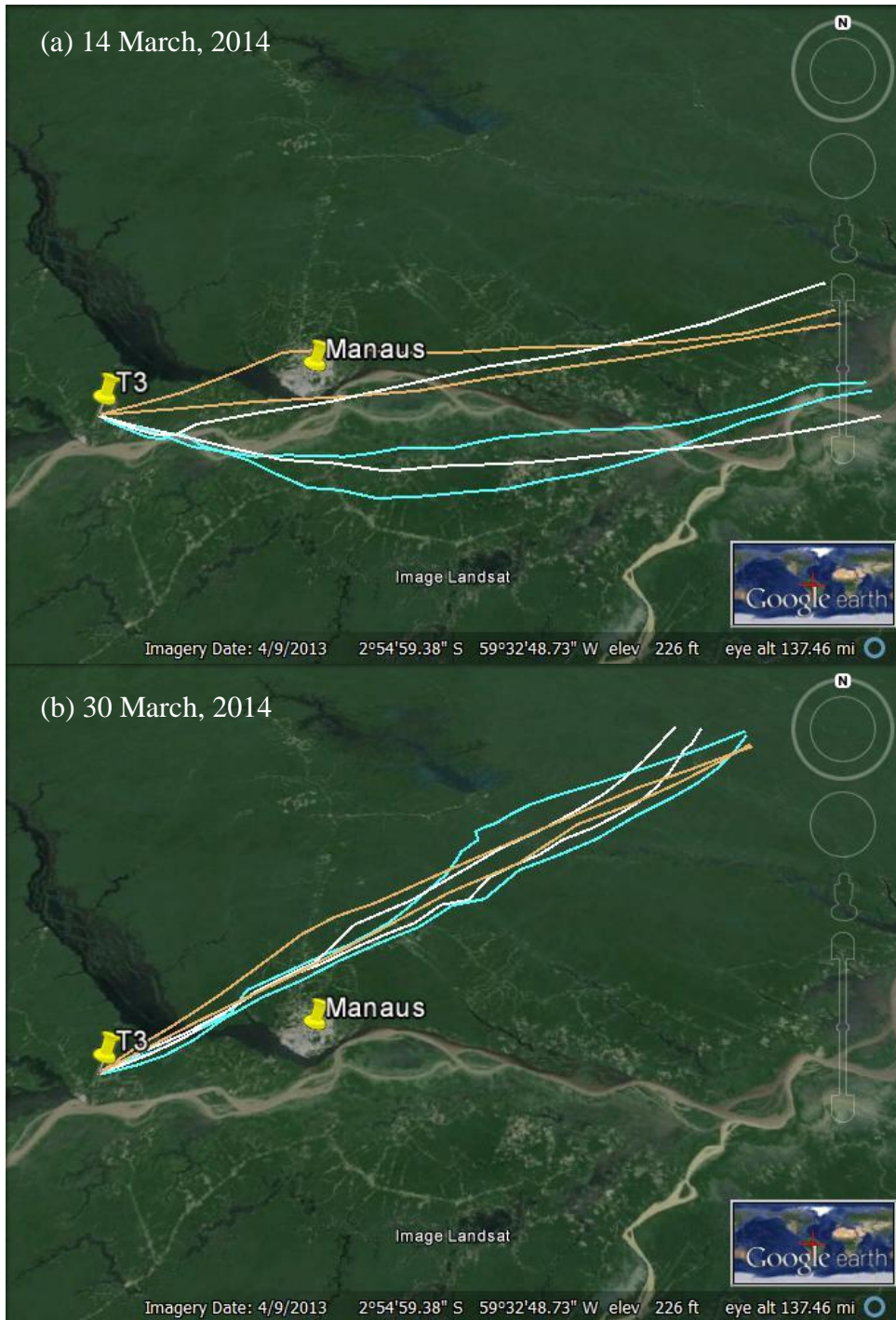


Figure S1

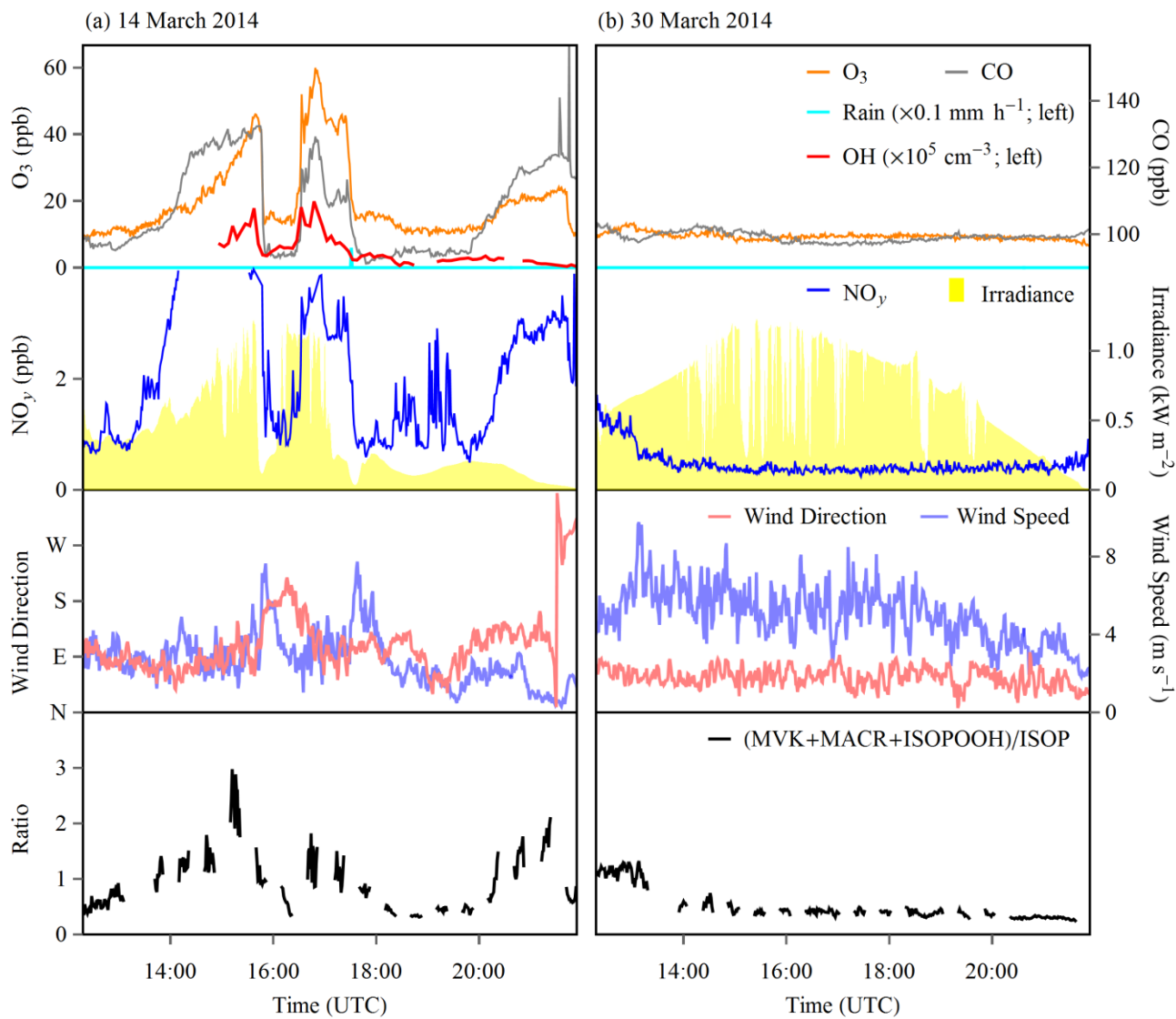


Figure S2

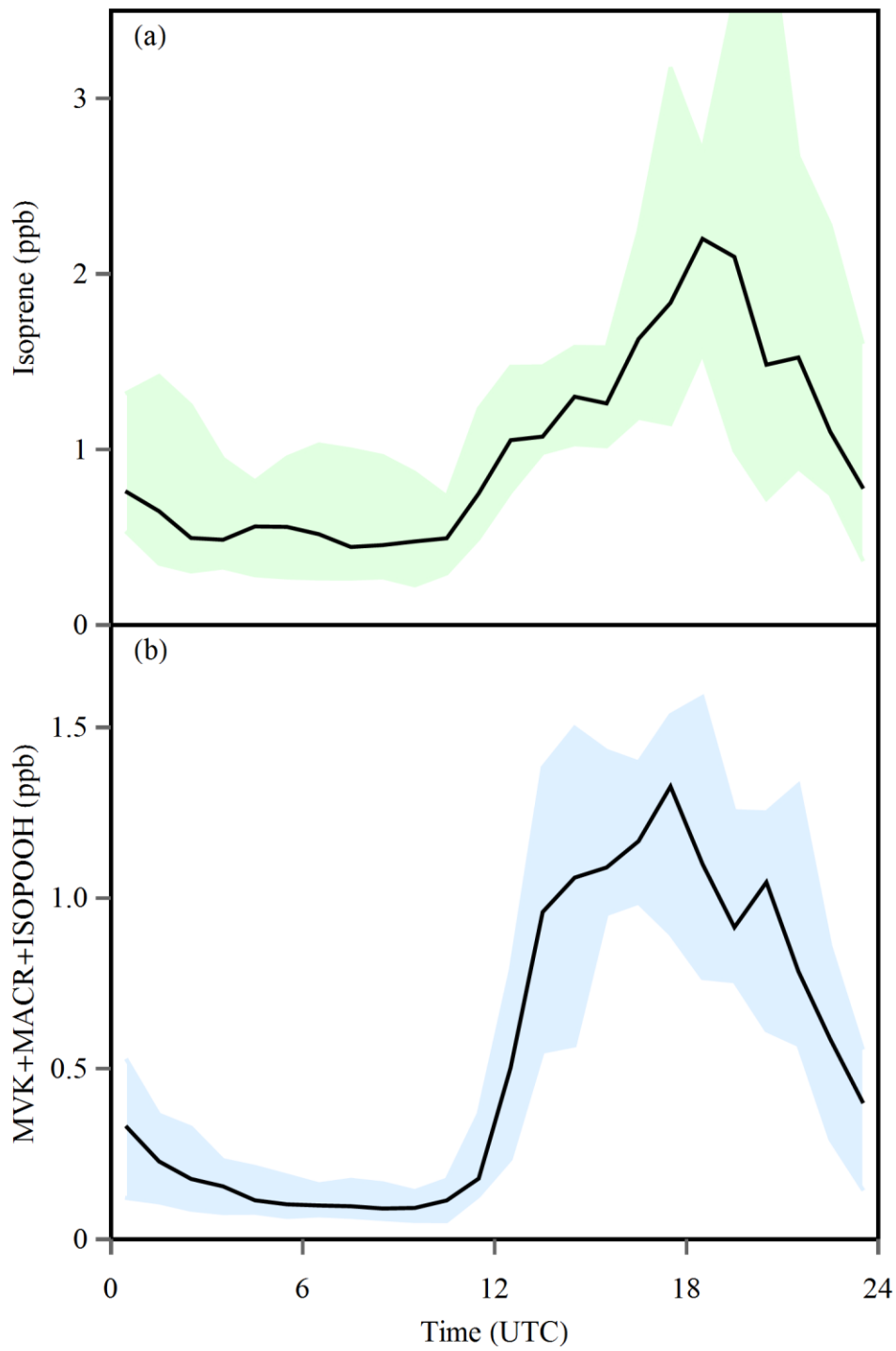


Figure S3

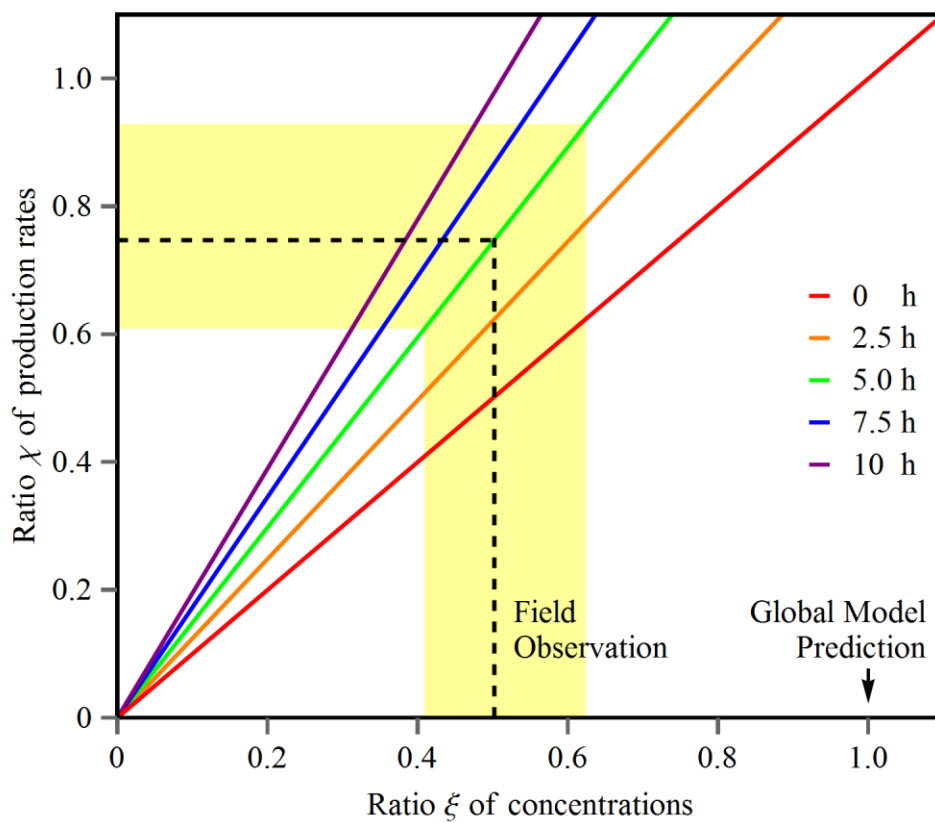


Figure S4

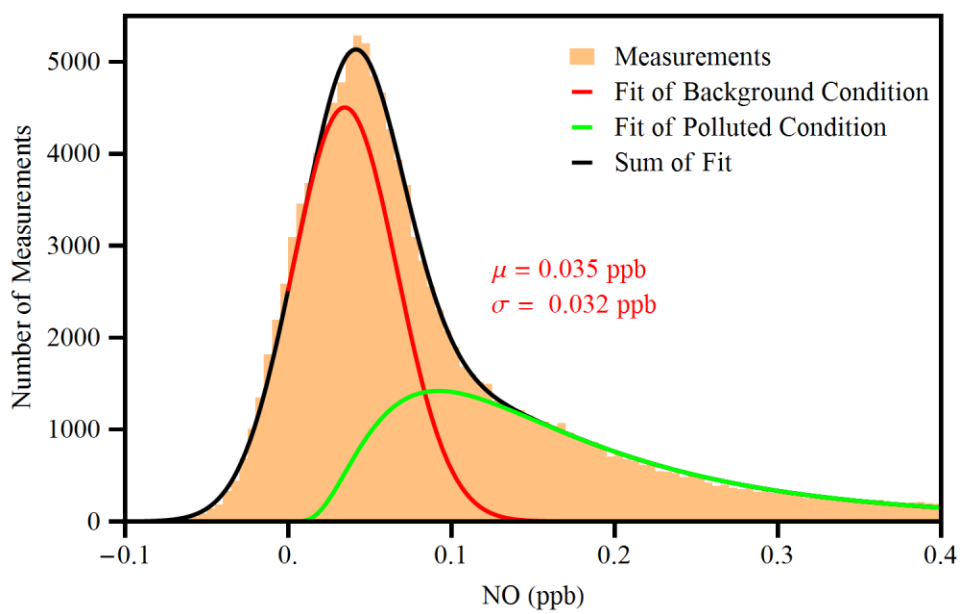


Figure S5

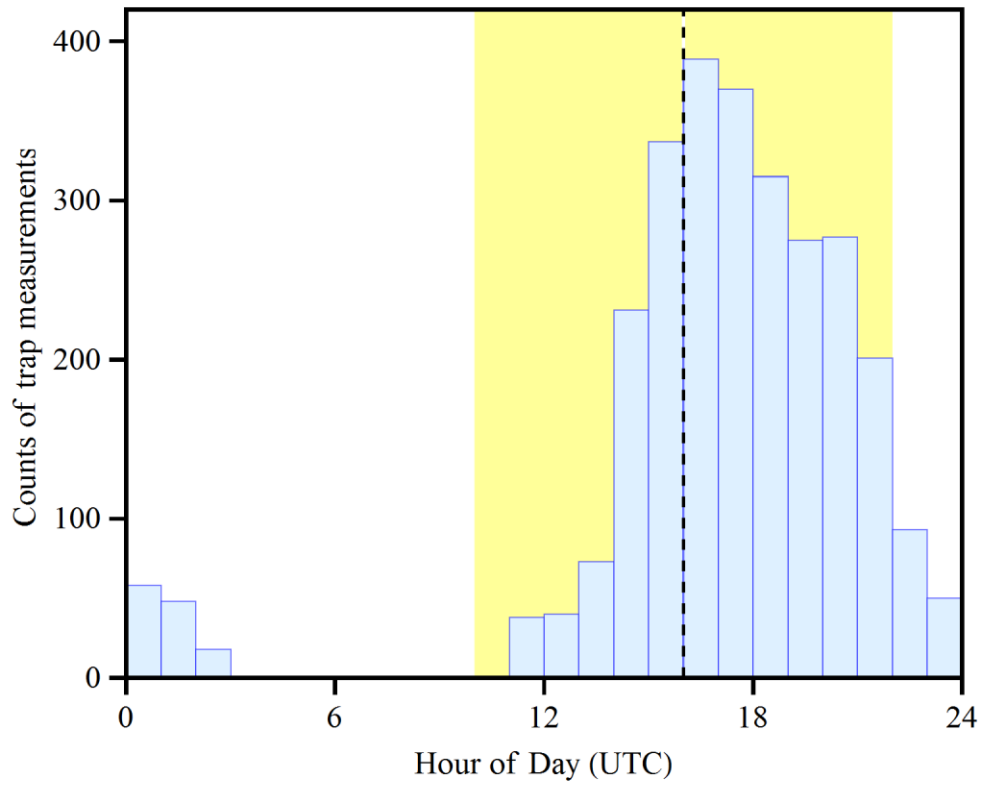
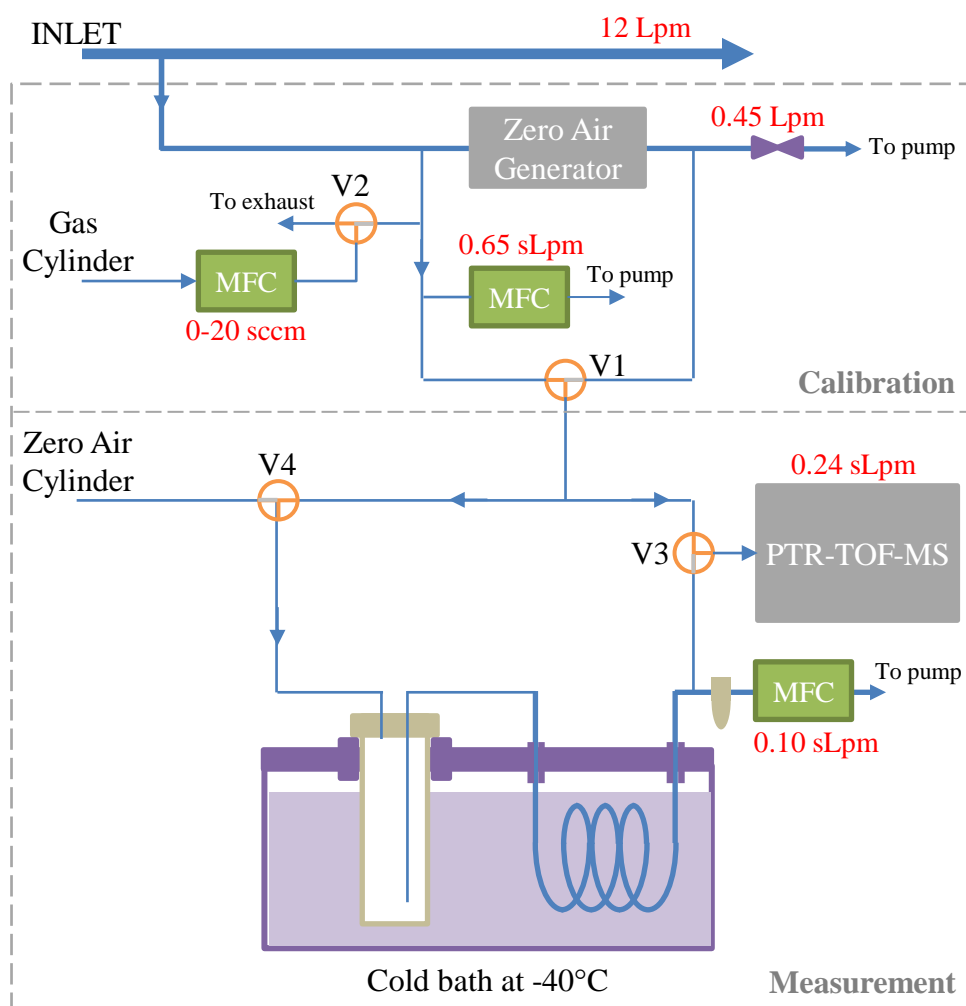




Figure S6



PFA tubing: — 1/2" (12.7 mm) — 1/4" (6.35 mm) — 1/8" (3.18 mm)

 Critical Orifice  Three-way valve (middle port is common


 Water Trap and grey port is normally closed)

Figure S7

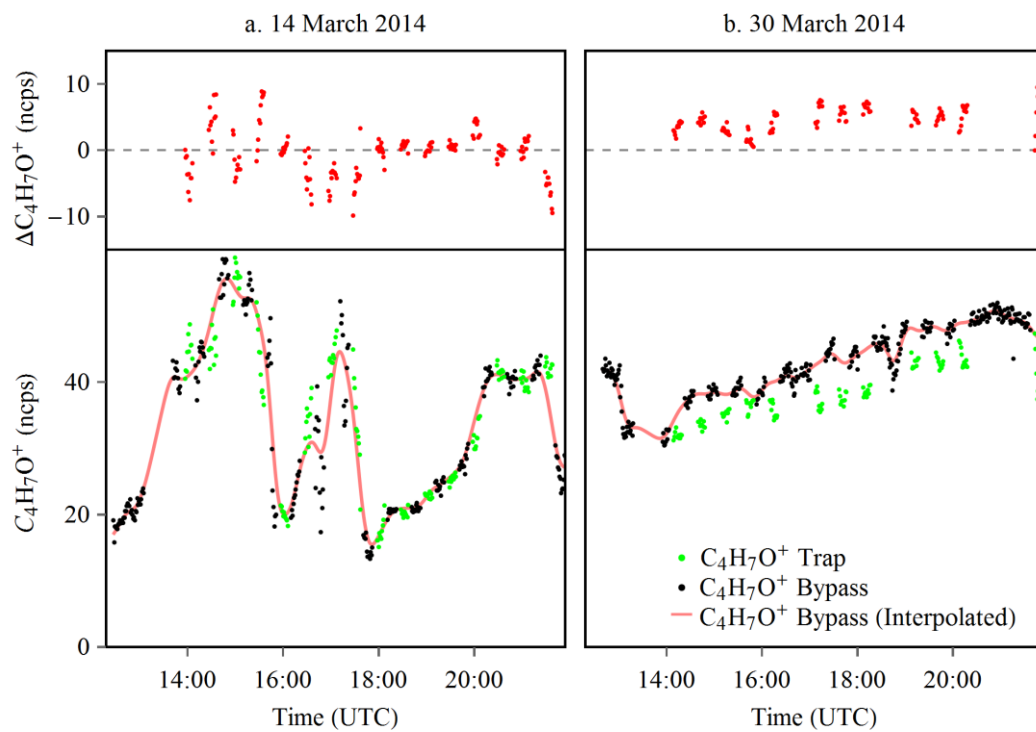


Figure S8

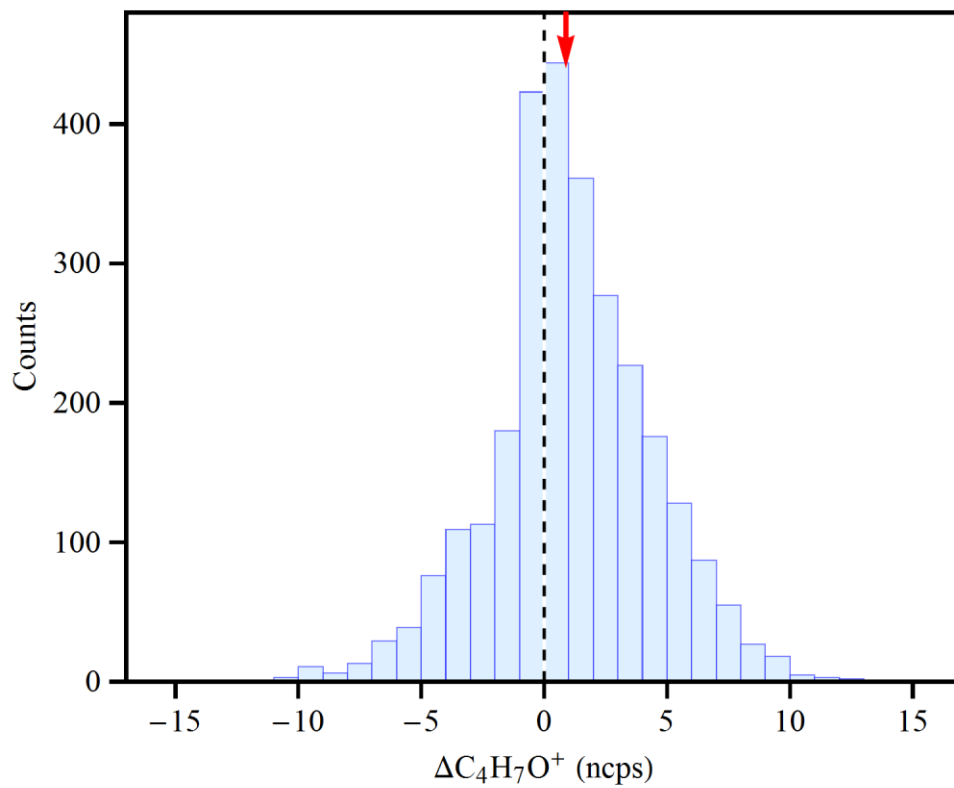


Figure S9

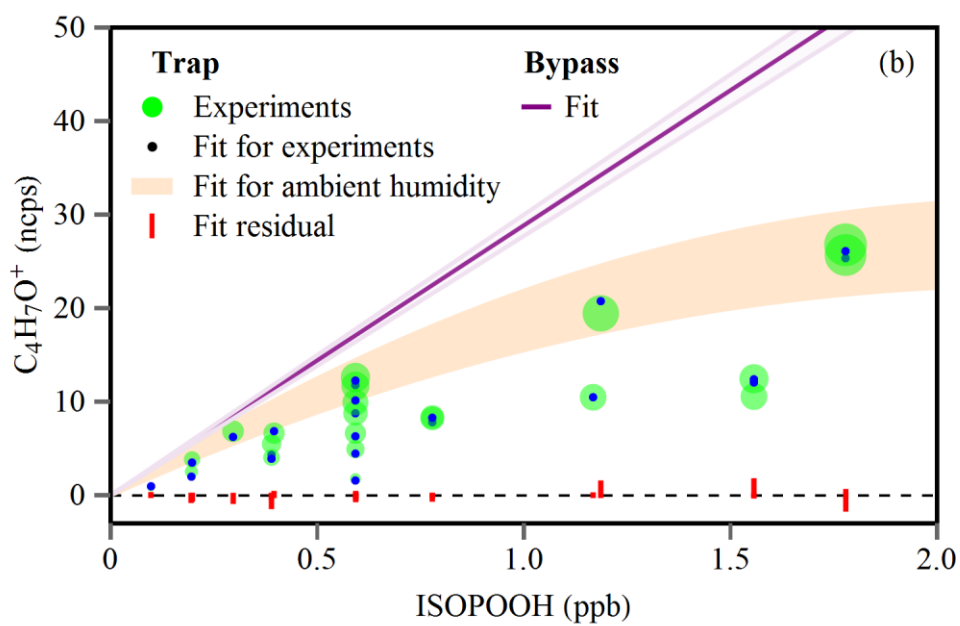
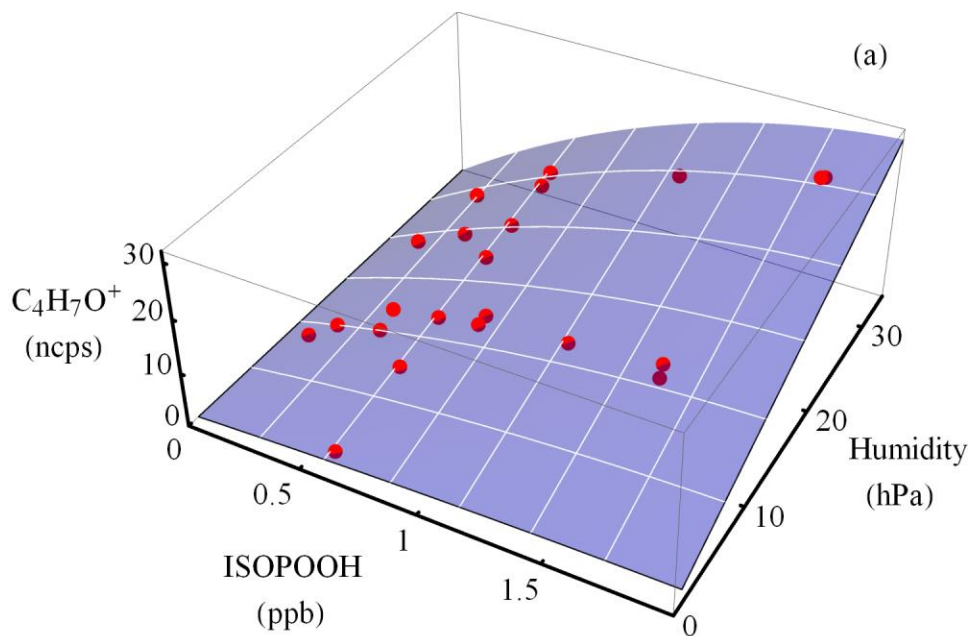


Figure S10

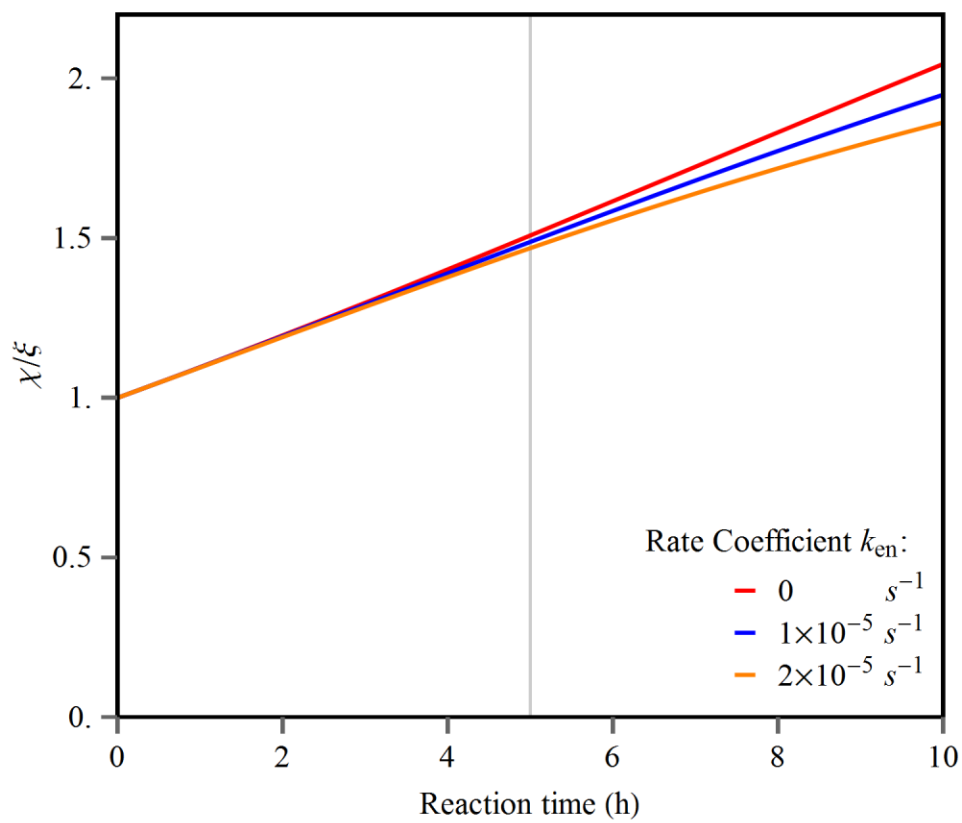


Figure S11

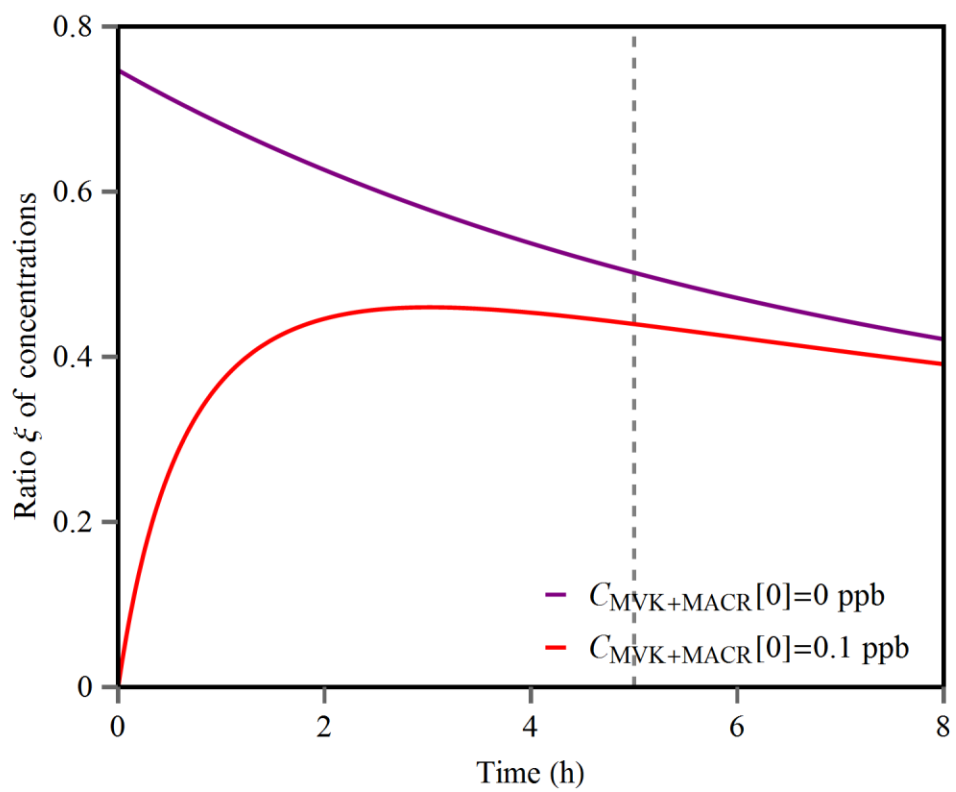


Figure S12

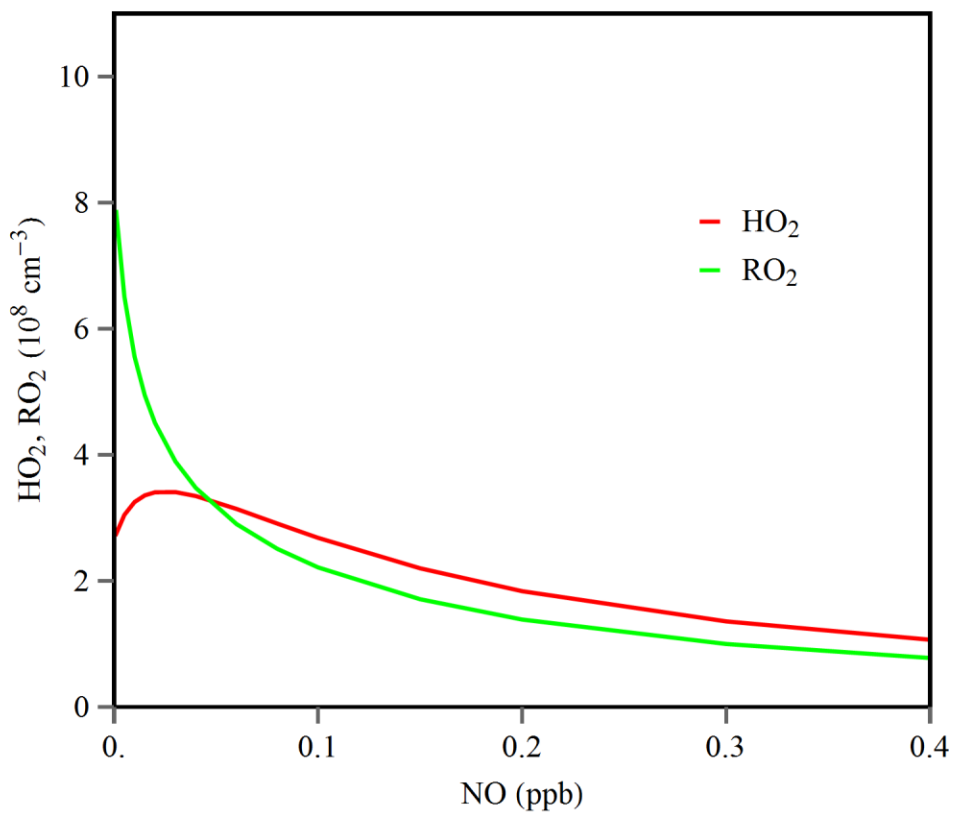


Figure S13